

# Learning-to-Learn the Wave Angle Estimation

Eray Güven, *Student Member, IEEE*, Güneş Karabulut Kurt, *Senior Member, IEEE*

**Abstract**—A precise incident wave angle estimation in aerial communication is a key enabler in sixth-generation wireless communication network. With this goal, a generic 3-dimensional (3D) channel model is analyzed for air-to-air (A2A) networks under antenna misalignment, radio frequency impairments and polarization loss. The unique aspects of each aerial node are highlighted and the few-shot learning as a model agnostic meta-learning (MAML) classifier is proposed for learning-to-learn (L2L) incident wave angle estimation by utilizing the received signal strength (RSS). Additionally, a more computationally efficient technique, first order model agnostic meta-learning (FOMAML) is implemented. It has been observed that the proposed approach reaches up to 85% training accuracy and 75.4% evaluation accuracy with MAML. Regarding this, a convergence rate and accuracy trade-off have been established for several cases of MAML and FOMAML. For different L2L models trained with limited data, heuristic accuracy performance is determined by an upper bound of the probability of confidence.

**Index Terms**—3-dimensional (3D) channel modeling, meta-learning, localization, aerial communication, model generalization.

## I. INTRODUCTION

Air-to-air (A2A) networks will play a crucial role in sixth-generation (6G) wireless communication networks. A2A enables continuous connectivity for aerial nodes over a wide area, leveraging line-of-sight (LoS) links, prompting the necessity of three-dimensional (3D) channel models for A2A networks for accurate performance evaluations [1]. Among the stochastic and deterministic 3D channel models, the impact of the antenna gain over the channel is an open issue that changes according to azimuth and elevation. We emphasize that assumptions of the ideal antenna and purely stable dynamic aerial node make the 3D channel models for A2A networks inapplicable. With a fixed on-board dipole antenna, a dynamic aerial node leads to dynamic antenna orientation. Under the antenna defects, polarization loss and antenna misalignment, the 3D channel model becomes more complex than 2-dimensional idealized channel models due to the spatial characteristic from the mobility and the additional dimension. Therefore, inherent 3D complexity hampers the utilization of critical applications over fading channels, such as incident wave angle estimation. The incident wave angle, also known as the angle of incidence, is the joint azimuth and elevation angles between the direction of the propagation and the normal to the surface of the antenna [2].

Determining the incident wave angle is valuable for beamforming, directional antenna placement, localization, interference mitigation, network planning, as well as smart antenna

This work was supported in part by the Natural Sciences and Engineering Research Council of Canada (NSERC) Discovery Grant program.

E. Guven and G. Karabulut Kurt are with the Department of Electrical Engineering, Polytechnique Montréal, Montréal, Canada, e-mail: {guven.era, gunes.kurt}@polymtl.ca

Table I. List of Parameters

Parameter	Description
$A_T^r, A_R^r$	Tx and Rx position in rectangular coord.
$U_T^r, U_R^r$	Tx and Rx rotation in rectangular coord.
$U_T^s, U_R^s$	Tx and Rx rotation in spherical coord.
$\tilde{U}_T^a, \tilde{U}_R^a$	Oriented Tx and Rx into a state of “a”
$\theta_R^r, \theta_R^p, \psi_R$	Roll, pitch and yaw for initial position
$\phi_R^{\psi, \theta}$	Incident wave angle with $\theta$ elevation and $\psi$ azimuth
$\tilde{\phi}_R^{\theta}$	Elevation component of the incident wave angle
$\tilde{\phi}_R^{\psi}$	Azimuth component of the incident wave angle
$\tilde{\phi}_R^{\theta}$	Estimated elevation component of incident wave angle
$\tilde{\phi}_R^{\psi}$	Estimated azimuth component of incident wave angle
$F_T^E, F_R^E$	$E$ -plane antenna pattern for Tx and Rx
$F_T^H, F_R^H$	$H$ -plane antenna pattern for Tx and Rx
$\zeta$	Antenna non-ideality factor
$D(\psi, \theta)$	Directivity of an antenna for $\phi_R^{\psi, \theta}$
$G(\psi, \theta)$	Gain of an antenna for $\phi_R^{\psi, \theta}$
$h_{\ell, k}^{\phi}$	$\ell$ -th tap on $k$ -th direction channel tap for $\phi_R^{\psi, \theta}$
$\kappa$	Rician $K$ - factor
$P_T$	Transmitted signal strength
$P_R$	Received signal strength
$p_\omega$	Incident wave vector
$p_A$	Rx antenna vector
$\mathcal{P}$	Polarization loss factor
$\hat{\theta}, \hat{\psi}$	Misaligned $\theta$ and $\phi$
$\delta_{T1}, \delta_{T2}$	Misalignment of Tx in $\theta$ and $\psi$
$\delta_{R1}, \delta_{R2}$	Misalignment of Rx in $\theta$ and $\psi$
$\text{MAML}(K, N)$	$N$ - class $K$ - shot MAML
$Q$	Meta-model parameter
$\hat{Q}$	Optimized meta-model parameter
$Q_{P_R}$	Meta-model parameter for RSS
$Q^\circ$	Meta-model parameter initialization
$\phi_{Q_{P_R}}^{\psi, \theta}$	Estimated $\phi^{\psi, \theta}$ using meta-objective of $Q_{P_R}$
$f_{Q_{P_R}}$	Meta-model classifier
$v_{(\phi_R^{\psi, \theta})}$	Meta-model classifier result
$\epsilon$	Meta model error tolerance
$\alpha_{\tilde{\phi}_R}$	Meta model confidence interval
$\alpha$	Meta-inner learning rate
$\beta$	Meta-step size

systems. It enables improved signal quality, enhanced system capacity, reduced interference, and more efficient use of wireless resources. Contemporary methods for incident wave angle estimation consist of the use of either pilots on transmission [3], or eigendecomposition of the received signal to subspace [4]. However, while the use of pilot signals reduces the maximum achievable rate, the eigendecomposition of the received signal becomes less effective due to the uncorrelated signal and known the number of path assumptions. Nevertheless, there are methods without requiring neither eigendecomposition nor additional pilots. Received signal strength (RSS) has been adopted in numerous studies for incident wave angle estimation, and it has been shown to be fairly successful [5].

Table II. Comparison of similar studies

	Antenna Modeling	Stochastic Channel Modeling	UAV Positioning	UAV Posture	Proposed Solution	Main Target Approach
[6]	MIMO / Ideal	Air-to-Ground Time-variant Rician Fading Channel Free Space Path Loss	Global Cartesian	Euler ZYX (Roll, Pitch and Yaw)	Model-based Neural Network (Closed-form expression)	Spatial Temporal Analysis (Unknown measurement and dataset)
[7]	MIMO / Ideal	Air-to-Air Time-variant Tapped Delay Line Channel No Path Loss	Local Cartesian	None (No Posture Design)	Time-variant scattering clusters	Spatial Temporal Analysis
[8]	MIMO / Ideal	Air-to-Ground Time-invariant Physical Channel No Path Loss	Global Cartesian	Euler ZYX (Roll, Pitch and Yaw)	Channel Estimation and Sensor Fusion with Integrated Sensing and Communication	Impact of Attitude Variation on Physical Channel
Ours	SISO / Ideal & Non-Ideal	Air-to-Air Time-Invariant Rician Fading Channel Log-normal Path Loss	Global Cartesian	Euler ZYX (Roll, Pitch and Yaw)	Model Agnostic Meta Learning (Open-form expression)	Incident Wave Angle Analysis

Note that the studies [9]–[11] exploit the RSS in incident wave angle estimation to have the ideal antenna with stationary nodes assumptions. It is clear that the utilization of RSS for incident wave angle estimation in dynamic aerial nodes under antenna defects is not an easy task. Not only does the antenna radiation field change with each rotation, but antenna defects disperse the field characteristics of the antennas in aerial nodes. In addition, the transmitter aerial node also suffers from this challenge as well. In this perspective, autonomous or remotely operated unmanned aerial vehicles (UAVs) are under examination as aerial nodes that serve within an A2A network.

As a solution to this complexity challenge, artificial intelligence (AI) approaches can be adopted to mitigate incident wave angle estimation errors. Neural network based AI algorithms has the capability to optimize non-convex problems, and supervised learning can be deployed to map each RSS value to corresponding incident wave angles [12]. Convolutional neural networks (CNN) have been used in many aspects of wireless communication for estimation, detection, and data compressing [13], [14]. Multiple studies show that channel adaptation of CNN is robust, although it fails in generalization for multi-task problems [15], [16]. Alternatively, densely connected neural networks (DenseNet) [17] with a large number of parameters are formidable tools for learning complex patterns yet, not immune to the issue of out-of-sample distribution and struggle with generalization and rapid adaptation. Therefore, reliance on memorization and susceptibility to overfitting can limit their effectiveness in facing with unseen scenarios. This leads to the search for new AI techniques that can create a generic AI model with limited data. Therefore, the RSS-aided incident wave angle estimation can be possible for any channel, antenna, and UAV conditions in A2A networks.

There are contemporary solutions that can avoid model overfitting when using the limited amount of data provided. Few-shot learning technique as meta-learning is a learning-to-learn (L2L) algorithm that enables rapid convergence using a limited amount of samples [18]. Meta-learning’s practical use was developed in 2016 as an imitation of the human mind that learns things it has not encountered before [19]. Forming a generic predictive model is possible with model-agnostic meta-learning (MAML) that can divide the incident wave angle estimation problem into several tasks [20]. By this way, an unknown task can be learned by the meta-optimization

across the tasks by stochastic gradient descent (SGD). Based on these, the generated black box model can be evaluated by any independent model for the incident wave angle estimation task. Guided by this concept, MAML offers both flexibility and interpretability for the RSS mapping into the incident wave angles.

#### A. Literature Review

A directly related study [21] examines the estimation of the direction of angle in array antennas with linear polarization. The importance of radiation patterns in aerial nodes has been highlighted in [22]. The study [23] examines the cross-polarization of various UAV antennas experimentally and highlights the UAV scattering effects on radiation efficiency. Another related study [24] proves that fuselage posture is a key criterion in UAV-to-vehicle (U2V) networks. A recent experimental air-to-ground study [25] shows that taking the UAV antenna radiation pattern into account increases localization accuracy. The multi sensor state estimation of UAVs is also an ongoing study. The studies [26] and [27] utilize sensor fusion to UAVs’ state estimation by inertial measurement sensors and global positioning system (GPS) information. State estimation with radio communication is a fresh topic, recently investigated in researches such as [28] and [29].

In this regard, the studies [17-24] primarily focus on the impact of antennas on UAV networks. While antennas are known to significantly impact aerial networks, existing studies often have limited consideration of antenna imperfections. For instance, [17] uses multi-mode multi input multi output (MIMO) antennas for the direction of arrival estimation, but the simulation-demonstration disparity is notable. Similarly, [18] and [19] discuss antenna issues such as cross-polarization, and [20] emphasizes the influence of fuselage posture on spatial-temporal correlations in a Rician fading aerial channel.

In our study, we push a step further in A2A communication by considering antenna imperfections in angle estimation. Recognizing the crucial roles that both the channel and signal quality play, we delve into their impact on localization. Utilization of RSS is substantial in incident wave angle estimation techniques [10], [30]. One study [31] examines the target localization by RSS and incident wave angle information only. Nevertheless, the dynamics of the UAVs are not taken into consideration for these studies. Nevertheless, maneuvering,

leading/following a trajectory, and wobbling are some common behaviors of all UAVs. Furthermore, it has been shown that the banana distribution of a hovering UAV motion is a special Gaussian distribution as well [32]. A recent study [33] highlights the fluctuation degradation and mobility angle impact over the link capacity for terahertz (THz) communication in A2A networks.

The use of few-shot learning was found to be very limited in wave characterization. Furthermore, the exploration of A2A network analysis in the context of UAV antenna imperfection remains a relatively unexplored and unaddressed domain within the scientific community. As a result, the potential effects of incident wave angle estimation in realistic scenarios have not been thoroughly investigated, leaving this aspect largely uncharted. Additionally, the application of AI to tackle and alleviate such challenges remains largely undiscovered, providing an opportunity for further research and innovative solutions in this field. In the sense of meta-learning usage in related topics, a recent study utilizes meta-learning in beam prediction problems for multiple input-single output (MISO) channel [34]. In a similar context, [35] exploits the meta-learning in maximization of the weighted sum rate problem for beamforming. One another study [36] uses meta-reinforcement learning to maintain user positions for virtual reality (VR) networks. One study makes use of the few-shot learning for multimodal target detection [37]. In [38], a first order model agnostic meta-learning (FOMAML) and almost no inner loop (ANIL) techniques have been used as autoencoder for RIS-assisted air-to-ground UAV networks. Evolution strategies for meta-learning variants such as reptile and meta-reinforcement are discussed in [39]. An overview of the communication techniques with the meta-learning technique is examined in [40]. In robotics, meta-learning is proposed for trajectory optimization in UAVs under challenging conditions [41]. Apart from the L2L field, usage of machine learning in beamforming technique is widespread, as in the contributions [42]–[44].

Two most related studies are compared in Table II with this research in terms of the methodology and the aim. Regarding the orientation formation, this study and [6] use the common terms of “elevation” and “azimuth” which only can be described with “ $Z - Y - X$ ” Euler representation in UAV posture definitions. In [6], a machine learning algorithm utilizes channel state information (CSI) such as path delays, path loss, shadow fading and Doppler shift. On the other hand, this study keeps a simple time invariant case to go deep further to generate a consistent dataset of RSS with a non-stationary quasi-static channel model, in order to estimate incident wave angles.

The use of RSS offers two distinct advantages. Firstly, being a non-complex value, it places less demand on the neural network, streamlining computational requirements. Secondly, the receiver UAV benefits from not having to engage in post-processing tasks, such as signal decryption which preserves privacy and saves from the over-the-air computation. In [7], the authors aims to introduce a geometry-based stochastic approach involving spatial dynamic clustering among UAVs. While the cluster evolves over time, the study does not account for UAV postures. Consequently, the maneuvers and rotations

of the UAVs are overlooked, and correlations rely solely on the arbitrary trajectory each UAV follows. However, our study, in alignment with findings from [6], shows that UAV posture is non-stationary and any rotation of the UAV body significantly influences signal quality.

Briefly, the existing literature lacks a comprehensive 3D channel model that incorporates antenna imperfections for dynamic A2A networks, as well as a solution for estimating the incident wave angle. The few available studies with meta-learning for incident wave angle estimation are limited in scope, as they do not explore both elevation and azimuth incident wave angles, and do not address the dynamic UAV antenna responses. In light of this research gap, this study aims to provide a thorough definition and a comprehensive solution for this unexplored area within A2A networks.

Based on the findings, this research makes the following contributions:

- Modeling a generic 3D channel model under antenna imperfections with polarization loss, antenna mismatches and antenna misalignment for A2A networks. Impacts of position and orientation are included.
- Proposing few shot meta-learning approach for estimating incident wave angles within an unknown channel by adopting a multitask learning perspective with limited RSS information. Meta-learning steps for MAML have been explicitly derived for the proposed incident wave angle estimation method. A custom dataset for the task optimization is created.
- Adopting a lower computational cost FOMAML technique in beam classification as an alternate to MAML and evaluating the impact of less gradient information on the incident wave angle estimation.
- Deriving a bound for the probability of confidence (PoC) of the generated AI models by Hoeffding’s inequality to justify their validity and reveal the requirement of meta-test dataset size for the desired success rate.
- Evaluating the generated models with the proposed dataset and demonstrating comparisons with each other, as well as the CNN model of MAML and more sophisticated DenseNet network.

## B. Organization and Notations

The rest of the paper is organized as follows. In Section II the system model with dynamic 3D-UAV integrated hardware and channel model has been introduced. In Section III, the challenges of the system and drawbacks within the contemporary solutions have been discussed. Next, Section IV establishes a collective task learning model with meta-learning in fast adaptation of any fading channel models. The numerical results have been discussed in Section V and the research directions that proposed model lead are listed in the Section VI. Finally, the conclusion of this study have been briefed in Section VII.

*Notation:* While bold letters have been denoted as matrices,  $\|\cdot\|_2$  indicates the  $L^2$  norm and  $\mathcal{CN}(0, \sigma^2)$  is the complex Gaussian distribution with zero mean and  $\sigma^2$  variance.  $\mathcal{U}(a, b)$  notates the uniform distribution with the lowest value  $a$  and



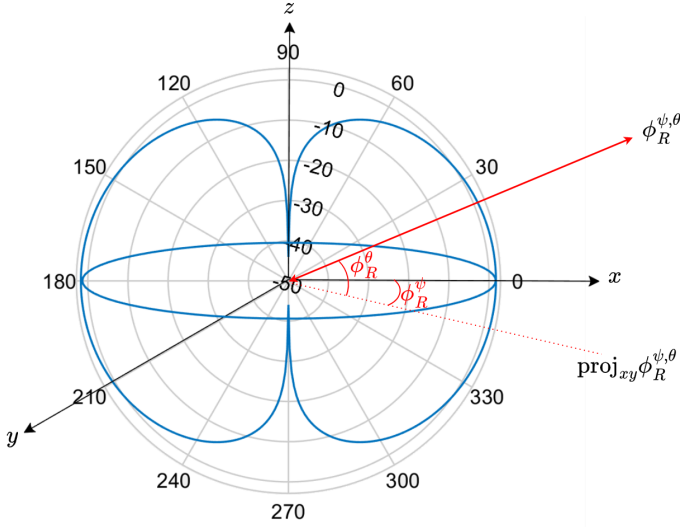


Figure 2. 3D representation of incident wave upon an ideal  $\mathbf{U}_{T,R}^r$  antenna radiation.

This completes the  $A \rightarrow B$ . Continuing on, the same logic repeats from point  $B$  to  $C$ . In this path, UAV takes the state of  $c$  for  $B \rightarrow C$  path as  $\tilde{\mathbf{U}}_{T,R}^c = \mathbf{R}^{cb} \mathbf{U}_{T,R}^b$ . Note that it has been assumed that receiver UAVs have the self-orientation information via inertial proprioceptive sensors. Based on these rotations, the radiation pattern of Rx with  $\tilde{\mathbf{U}}_{T,R}^a$  can be defined with the decomposition of the principal patterns of  $E$ - plane and  $H$ - plane components in GRF as following

$$\mathbf{F}_{T,R}(\psi, \theta, \zeta) = [F_{T,R}^E(\psi, \theta, \zeta), F_{T,R}^H(\psi, \theta, \zeta)]^\top. \quad (3)$$

The antenna follows additive  $\zeta \sim \mathcal{N}(0, \sigma_\zeta^2)$  impairment model for sourced by fabrication and reflections that will be discussed in Section III-C. Showing the dynamic model of antenna position and orientation in Cartesian coordinates, A2A distance is defined as  $d = \|\mathbf{A}_T^r - \mathbf{A}_R^r\|_2$  and  $\phi_R^\psi = \arctan(\frac{d_y}{d})$  and  $\phi_R^\theta = \arctan(\frac{d_z}{d})$ . Since the antenna pattern covers in  $(0, 2\pi]$  azimuth field of view is equal in an ideal case,  $\phi_R^\theta$  will be the main concern of this study. The probability of UAV's position is considered as uniform distribution with near-field constraint ( $d_{\min}$ ) and coverage limit ( $d_{\max}$ ) where

$$p_d(d) = \frac{1}{d_{\max} - d_{\min}}, \quad [d_{\min} < d < d_{\max}]. \quad (4)$$

As a result, the distribution of  $p_{\phi^\theta}(\phi^\theta|d)$  can be obtained with transformation density function as

$$\begin{aligned} p_{\phi^\theta}(\phi^\theta|d) &= p_d \left( \frac{d_z}{\tan(\phi^\theta)} \right) \left| \frac{\partial d}{\partial \phi^\theta} \right|, \\ &= p_d \left( \frac{d_z}{\tan(\phi^\theta)} \right) |d_z \csc^2(\phi^\theta)|, \\ &= \frac{d_z}{d_{\max} - d_{\min}} \csc^2(\phi^\theta), \end{aligned} \quad (5)$$

where  $\phi^\theta$  is denoted by  $\{\phi^\theta \in \mathbb{R} : \arctan(\frac{d_z}{d_{\min}}) < \phi^\theta < \frac{\pi}{2}\}$ . With the linear primary polarization, the limitations in the gain ( $G$ ) can be obtained with the knowledge of transmission  $\phi_T^{\psi, \theta}$  and incident wave angles  $\phi_R^{\psi, \theta}$ .

**Lemma 1.** A short dipole antenna with  $L \ll \frac{\lambda}{2}$ , the radiation intensity ( $U$ ) is a function of the electric field  $E_\theta$  in far-field radiation region and therefore the directivity is a function of  $\phi_{T,R}^\theta$  as following

$$\begin{aligned} D(\psi, \theta) &= 4\pi \frac{\max U(\psi, \theta)}{P_r} = 4\pi \frac{\max U(\theta)}{P_r}, \\ G(\psi, \theta) &= D(\psi, \theta). \end{aligned} \quad (6)$$

*Proof.* See Appendix A.

## B. Channel Model

An accurate estimation of incident wave angle offers the feasibility of adapting the angle varying channel. A SISO configured A2A link is considered for this study. Both uplink and downlink transmissions are taken into account during the 3D channel forming. Channel vector has a dependency on the  $\phi_R$  denoted as  $\mathbf{h}_k^\phi \in \mathbb{C}^{1 \times N}$  where  $N$  is the number of multipath components (MPC). The system model to be described holds true for bidirectional propagation, as both the channel and the antenna are reciprocal. In this respect, the communication direction is denoted by a transmission index  $k = \{1, 2\}$ . The received signal  $y_k^\phi$  can be shown as follows

$$y_k^\phi = h_k^\phi x_k + n_k^\phi, \quad (8)$$

where  $x_k$  is the transmitted signal,  $\mathbf{n}_k^\phi \sim \mathcal{CN}(0, \sigma^2)$  is the complex additive white Gaussian noise (AWGN). With the assumption of having an LoS link, the frequency selective Rician fading channel with MPC under an LoS link has been considered for this study. Due to the predominant LoS path, the Rician fading channel model is used which also takes the scattering and multipaths account. Therefore, a discretized  $L$ -tap baseband model with bandwidth  $W$  and  $m/W$  sampling, baseband channel  $g_{\ell,k}$  can be shown as following [45]:

$$g_{\ell,k}[m] = \sum_i a_i(m/W) e^{-j2\pi f_c \tau_i(m/W)} \text{sinc}[\ell - \tau_i(m/W)W], \quad (9)$$

where  $f_c$  is the centre frequency, the gains of  $\ell$ -th tap is  $a_i$  and propagation delay is  $\tau_i$  follows uncorrelated wide-sense stationary scattering within single tap. Thence, the distribution of cumulated independent filter taps forms a Rician fading with  $\kappa$ -factor can be written as

$$g_{\ell,k}[m] = \sqrt{\frac{\kappa}{\kappa+1}} \sigma_\ell e^{j\xi} + \sqrt{\frac{1}{\kappa+1}} \mathcal{CN}(0, \sigma_\ell^2), \quad (10)$$

where the first term includes the incident wave characteristics ( $\xi$ ) of the LoS component while the second term is the circular symmetric cumulated diffuse components, independent from the first LoS component, therefore the  $\phi^{\psi, \theta}$ . Expanding the  $\xi$ , channel of an LoS incident wave angle under dynamic antenna configuration with  $\mathbb{E}[|g_{\ell,k}|^2] = 1$  can be described with as following

$$\begin{aligned} g_{\ell,k}^\phi[m] &= \sqrt{\frac{\kappa}{\kappa+1}} \sigma_\ell \exp\{j2\pi f_D \cos(\phi_R^{\psi(\cdot), \theta}) + \varphi\} \\ &\quad + \sqrt{\frac{1}{\kappa+1}} \mathcal{CN}(0, \sigma_\ell^2), \end{aligned} \quad (11)$$

$$\mathbf{R}_x(\Theta_3) = \begin{pmatrix} 1 & 0 & 0 \\ 0 & \cos(\Theta_3) & -\sin(\Theta_3) \\ 0 & \sin(\Theta_3) & \cos(\Theta_3) \end{pmatrix}, \mathbf{R}_y(\Theta_2) = \begin{pmatrix} \cos(\Theta_2) & 0 & \sin(\Theta_2) \\ 0 & 1 & 0 \\ -\sin(\Theta_2) & 0 & \cos(\Theta_2) \end{pmatrix}, \mathbf{R}_z(\Theta_1) = \begin{pmatrix} \cos(\Theta_1) & -\sin(\Theta_1) & 0 \\ \sin(\Theta_1) & \cos(\Theta_1) & 0 \\ 0 & 0 & 1 \end{pmatrix} \quad (7)$$

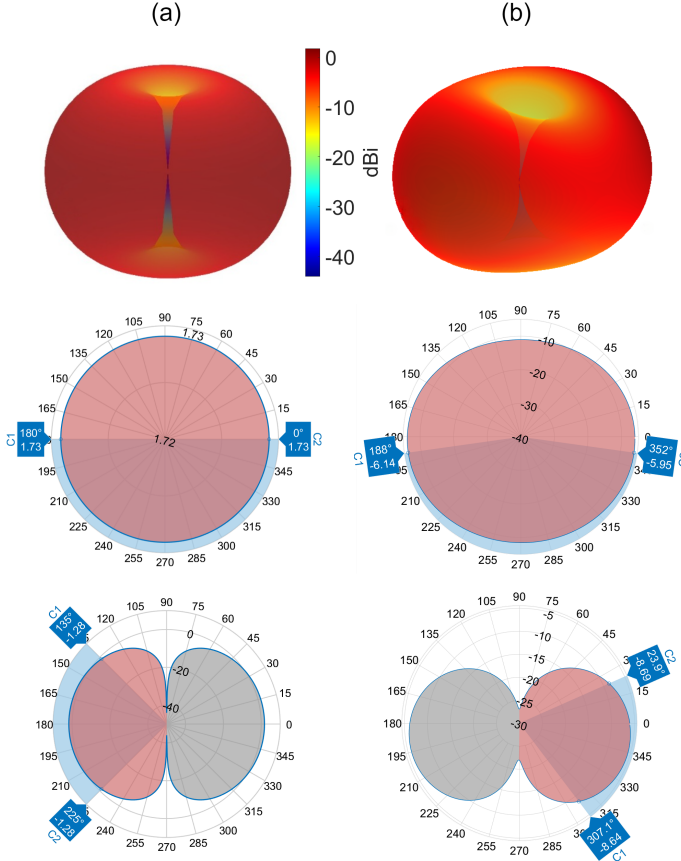


Figure 3. Impact of antenna imperfection to the radiation pattern. a) Ideal Antenna vs. b) Non-ideal antenna with  $\zeta$  impairment.

where  $f_D$  denotes the maximum Doppler frequency,  $\phi_R^{\psi(\cdot),\theta}$  is the incident wave angle with  $\theta$  and arbitrary azimuth angle  $\psi$ , and  $\varphi$  is the phase. The UAV azimuth rotations around  $z$ -axis impact for  $P_R$  can be neglected on GRF such that  $F_R(\psi_R^i, \theta_R^{(a)}) = F_R(\psi_R^j, \theta_R^{(b)})$ ,  $\forall i, j$  if and only if  $\theta_R^{(a)} = \theta_R^{(b)}$ . Therefore, the fading channel by using the predefined geometry for A2A becomes,

$$g_{\ell,k}^\phi[m] = \sqrt{\frac{\kappa}{\kappa+1}} \sigma_\ell \exp\left\{j2\pi f_D \cos\left(\arctan\left(\frac{d_z}{d}\right)\right) + \varphi\right\} + \sqrt{\frac{1}{\kappa+1}} \mathcal{CN}(0, \sigma_\ell^2). \quad (12)$$

For the large scale fading model, outdoor log-distance path loss is defined as

$$\text{PL (dB)} = \text{PL}_0 + 10\eta \log_{10}\left(\frac{d}{d_0}\right) + X_g, \quad (13)$$

where  $d_0$  is the reference distance,  $\text{PL}_0$  is the free-space path loss in dB,  $d$  is the length of path,  $\eta$  is the path loss exponent and  $X_g \sim \mathcal{CN}(0, \sigma_p^2)$  is the fading loss by the described channel model. The corresponding large-scale average channel gain for the  $\ell$ -th tap is  $c_{\ell,k}[m] = d^{-\eta} 10^{\frac{-\text{PL}_0}{10}}$ , independent of the  $\phi^{\psi,\theta}$ . Thus, the accumulated channel for two-way channel with  $\phi^{\psi,\theta}$  incident wave is following

$$h_{\ell,k}^\phi[m] = \sqrt{c_{\ell,k}[m]} g_{\ell,k}^\phi[m]. \quad (14)$$

Simply, RSS is defined as  $P_R = P_T - \text{PL}$  at the Rx UAV. The SNR for such a two-way A2A with  $\phi^{\psi,\theta}$  link model without interference can be defined as following,

$$\text{SNR}_{\ell,k}^\phi = \frac{P_T |h_{\ell,k}^\phi|^2 G(\psi, \theta)}{\sigma^2}, \quad (15)$$

where  $|h_{\ell,k}|^2$  is the channel gain at the corresponding node.

### III. AN OVERVIEW OF THE IMPAIRMENTS AND ESTIMATION PROBLEMS

As one of the main focuses for localization application requirements, incident wave angle estimation by using time-of-flight (ToF) techniques such as time difference of arrival (TDoA) between the aerial nodes is quite affordable to implement. However, extracting the elevation and azimuth angles out of the incident wave angle is also an estimation problem to solve that has been discussed in [46], [47]. Apart from the estimation errors, the proposed methods in those studies are defined under some constraints (e.g. randomness of the positions in the array elements, only viable in a limited span). The root of this fundamental problem which is the propagation direction of the incident wave of the UAV node can be found by the RSS. With the conventional methods [9], minimum differential RSS ( $\Delta P_R$ ) leads to the incident wave angle for the reference plane. Note that  $\mathbf{P}_R = [P_R^{(1)}, \dots, P_R^{(K)}]^\top$  and  $\Delta P_R = P_R^{(i)} - P_R^{(j)}$ . For the vertically polarized short dipole antenna, minimized  $\Delta P_R$  with the corresponding maximum power  $\Lambda(\phi) = |F_R^E(\psi, \theta, \zeta)|^2$  that leads to the  $\hat{\phi}_R$  solution modeled as the following,

$$C(\phi) = \frac{1}{\|\Lambda(\phi) - \Delta P_R\|_2^2}. \quad (16)$$

where  $\Lambda(\phi) \subset \Lambda(\phi)$  and  $\Delta P_R \subset \Delta P_R$ . As a result, the estimated  $\hat{\phi}_R$  is following

$$\hat{\phi}_R = \arg \max_{\phi_R \in \Phi_R} C(\phi). \quad (17)$$

With this approach, Tx orientation  $\tilde{\mathbf{U}}_T^b$  is not required to be known by the Rx, simply can be estimated with the RSS maximization algorithm for ideal Tx and Rx antennas.

There are many major challenges to having an accurate  $\hat{\phi}_R$  for A2A networks. Among the ToF techniques, one essential need for TDoA is the *synchronization* of sensor clocks in universal time during the localization process. Another requirement is the *zero misalignment* between the aerial nodes, which is difficult to conceptualize in A2A networks. Conventional AI with data driven methods is not a feasible solution since  $p_{\phi^\theta}(\phi^\theta|d)$  for each trajectory sets in  $\mathcal{S}$  with a different distribution which only can be defined as a new task. As a result, each solution offered therefore brings with it another problem and/or constraint. We search for a way to approach the most generic solution with the minimum amount of dependency in A2A networks that contain hardware challenges from a 3D channel perspective. Then we evaluate the generalized model for incident wave angle estimation in 3D channel models exposed by the antenna defects and imperfections.

Some main concerns related to antenna imperfections namely polarization loss due to antenna mismatches, antenna misalignment and RF impairments due to the reflections and fabrication errors are described in the following subsections. “A general comment can be made that the results of the impairment models are influenced by aggregated independent non-idealities, leading to propagated errors.” Accordingly, the impact of the antenna imperfections in investigated with their direct results on the system model. Firstly, the orientations of UAVs result in polarization loss, only if the orthogonality between the antenna and incident wave angle is broken down. Secondly, the positioning of the UAVs may result within 2 different scenarios. 1) UAVs are aligned but not orthogonally placed on the space (due to a path trajectory or mobility model) intentionally and 2) UAVs are not aligned to each other due to maneuvering and wobbling unintentionally on any placement. On both scenarios, the misalignment results in the radiation loss on the received signal. Therefore, we kept our investigation on polarization, misalignment and fabrication losses which ultimately covers any loss scenarios.

### A. Polarization Efficiency

The polarization matching in LoS links in A2A communication becomes a significant challenge considering the UAV rotations. Only vertical or horizontally polarized antenna transmissions with rotation on the orthogonal axis will lead to polarization loss. Considering the impact on the  $P_R$ , this loss determines the throughout impact of the mismatch, without requiring to deep through analysis [21] of field polarization for each plane. Antenna polarization impact on both  $\mathbf{U}_T^r$  and  $\mathbf{U}_R^r$  can be investigated on the same coordinate system as the polarization vector of the wave. The polarization loss factor (PLF) can be defined as

$$\mathcal{P} = |p_\omega p_A|^2, \quad (18)$$

where  $p_\omega \in \mathbb{R}$  is the incident wave polarization,  $p_A \in \mathbb{R}$  is the receiver antenna polarization vector and  $0 \leq \mathcal{P} \leq 1$ . On the 3D perspective with  $\hat{\theta}_R$  and  $\hat{\psi}_R$  antenna misalignment components, the PLF for linearly polarized antenna components can

be shown as

$$\begin{cases} \mathcal{P}_\psi = \mathbf{U}_{T,R}^{r, \text{PLF}(\psi)} = \cos^2 \hat{\psi}_R, \\ \mathcal{P}_\theta = \mathbf{U}_{T,R}^{r, \text{PLF}(\theta)} = \cos^2 \hat{\theta}_R. \end{cases} \quad (19)$$

As a result, the weakened received signal by the PLF denoted as following

$$P_R^\dagger = \mathcal{P}_\psi \mathcal{P}_\theta P_R. \quad (20)$$

For example, it is more than enough to have one orthogonal axis rotation with respect to  $\mathbf{U}_R^r$  to maximize the PLF. In addition, these impairments have an impact on each other. “On the ideal case of polarization loss factor (PLF), heading (yaw axis) of the short dipole UAV antennas does not change the orthogonality between two UAV nodes since  $\mathbf{F}_{T,R}(\psi, \theta) = \mathbf{F}_{T,R}(\psi + \delta\psi, \theta)$ . However, this is not the case on non-ideal antenna, where  $\mathbf{F}_{T,R}(\psi, \theta, \zeta(\psi, \theta)) \neq \mathbf{F}_{T,R}(\psi + \delta\psi, \theta, \zeta(\psi + \delta\psi, \theta))$ . With an unbiased impairment assumption, the antenna omnidirectivity allows the yaw independency for the large amount RSS instance [48] if and only if  $\delta \sim \mathbb{N}(0, \sigma_\delta^2)$ :

$$\mathbb{E}[\mathbf{F}(\psi \pm \delta, \theta)] = \mathbb{E}[\mathbf{F}(\psi, \theta)] \pm \mathbb{E}[\mathbf{F}(\delta, 0)] = \mathbf{F}(\psi, \theta). \quad (21)$$

### B. Antenna Misalignment

Antenna misalignment can be defined for two different scenarios. First, it occurs by the elevation disequilibrium in A2A link such that  $d_{\mathbf{u}_T} \hat{\mathbf{u}} \neq d_{\mathbf{u}_R} \hat{\mathbf{u}}$  where  $\hat{\mathbf{u}}$  is the unit vector in the direction of the corresponding antenna. Second, independent from the altitude difference, misalignment occurs when an aerial node misaims the radiation field where UAV’s actual orientation or attitude does not match the desired or commanded orientation such that  $\tilde{\mathbf{U}}_T^a \neq \tilde{\mathbf{U}}_R^a$  for any  $\mathbf{R}_z(\Theta)$  on  $\mathbf{U}_{T,R}$ . Under the  $\pm\delta$  misalignment for all planes, the SNR of this model is the following

$$\widetilde{\text{SNR}}_{\ell,k}^\phi = \frac{P_T |h_{\ell,k}|^2 G_T(\theta \pm \delta_{T1}, \psi \pm \delta_{T2}) G_R(\theta \pm \delta_{R1}, \psi \pm \delta_{R2})}{\sigma^2}. \quad (22)$$

The derivation of the next step of Eq. (22) uses the property as following below:

$$D_T(\theta_i, \psi_j) = D_T(\theta_i, \psi_k) \forall i, j, k \quad (23)$$

$$D_R(\theta_i, \psi_j) = D_R(\theta_i, \psi_k) \forall i, j, k \quad (24)$$

Therefore,  $G(\theta_i, \psi_j) = G(\theta_i, \psi_k)$  if the radiation efficiency is 1. Thus,  $G(\theta_i, \psi_j + \delta_{T2}) = G(\theta_i, \psi_j)$  for both Tx and Rx. In this case, the neutral element of  $\psi$  can be dropped from  $\widetilde{\text{SNR}}_{\ell,k}^\phi$  which turns into the following:

$$\widetilde{\text{SNR}}_{\ell,k}^\phi = \frac{P_T |h_{\ell,k}|^2 G_T(\theta \pm \delta_{T1}) G_R(\theta \pm \delta_{R1})}{\sigma^2}. \quad (25)$$

That is, azimuth misalignment in BRF has no impact on the RSS level in an ideal short dipole while the elevation misalignment caused by both altitude and attitude mismatches have a direct relationship with the RSS and therefore the SNR.

### C. Antenna with RF Impairments and Defects

Due to the fabrication [49] and finite length antenna placement on UAV board [50], [51], antenna imperfections can

be encountered and these flaws can be seen in the antenna field pattern. A comparative analysis was conducted between an ideal and non-ideal short dipole antenna, as illustrated in the Figure 3. Once the antenna response becomes defective, the antenna possesses some directional antenna characteristics such as main lobe, back lobe and side lobe levels (SLL). Furthermore, the HPBW intervals on elevation angle are not  $[\frac{\pi}{4}, \frac{-\pi}{4}]$  and  $[\frac{3\pi}{4}, \frac{5\pi}{4}]$  anymore. On top of this,  $G_{\max}$  depends on both planes in non-ideal antennas, unlike the ideal case where  $G_{\max}$  depends on the elevation cut solely. Under the previously defined Eq. (3) defective antenna, an *i.i.d.* multivariate AWGN of  $\zeta$  for each plane has been defined as follows

$$D_{E,H} = \begin{bmatrix} D_E \\ D_H \end{bmatrix}, \mu_\zeta = \begin{bmatrix} D_H(\psi) \\ D_E(\theta) \end{bmatrix}, \Sigma_\zeta = \begin{bmatrix} \sigma_\psi^2(\psi) & 0 \\ 0 & \sigma_\theta^2(\theta) \end{bmatrix} \quad (26)$$

In the following steps,  $G(\psi, \theta)$  can be calculated without loss of generality. Note that  $\zeta$  impairments in the antenna also aggregate the error in misalignment mentioned in the previous section. The probability distribution for  $\zeta$  is simply,

$$p(x; \mu_\zeta, \Sigma_\zeta) = \frac{1}{2\pi |\det(\Sigma_\zeta)|} \exp\left(-\frac{1}{2}(x - \mu_\zeta)^\top \Sigma_\zeta^{-1}(x - \mu_\zeta)\right). \quad (27)$$

As described in Section II,  $\zeta$  will be an additive random variable on  $(0, 2\pi]$   $E$ -plane and  $(0, \pi]$   $H$ -plane. With the modified HPBW for each plane, the sum directivity becomes [52]

$$\frac{1}{D_{\text{sum}}} = \frac{1}{2} \left[ \frac{1}{D_E} + \frac{1}{D_H} \right], \quad (28)$$

where

$$D_E \simeq \frac{1}{\frac{1}{2 \log 2} \int_0^{\Omega_E/2} \sin \theta d\theta} \simeq \frac{16 \log 2}{\Omega_E^2}, \quad (29)$$

$$D_H \simeq \frac{1}{\frac{1}{2 \log 2} \int_0^{\Omega_H/2} \sin \theta d\theta} \simeq \frac{16 \log 2}{\Omega_H^2}, \quad (30)$$

where  $\Omega_H$  and  $\Omega_E$  are HPBW of corresponding planes in radian. Turning back to the example in Figure 3, under a Gaussian impairment for both planes as defined in Eq. (3), a 20 MHz centre frequency operating ideal antenna responses in Figure 3(a) can transform into the Figure 3(b). In this example, HPBW shrank from  $90^\circ$  to  $76.8^\circ$ , the main lobe acquired  $-5.55$  dB at  $344^\circ$  and the back lobe has  $-7.68$  dB at  $164^\circ$ . Note that the same field pattern flaws are valid for both transmitter and receiver antennas due to the antenna reciprocity.

#### IV. META-LEARNING SOLUTIONS

The problem arises from the estimation of  $\phi_R^{\psi, \theta}$  when  $|\phi_T^\theta - \phi_R^\theta| \neq 0$  leads to  $\hat{\phi}_R^\theta \neq \angle \max\{\hat{P}_R\}$  due to the MPC and antenna imperfections under the assumption of  $\hat{P}_R \xrightarrow{p} P_R$ , yet the solution is possible for some  $\tilde{\mathbf{U}}_{(T,R)}^a = \mathbf{R}^{ab} \mathbf{U}_{(T,R)}^b$  exist. The non-zero correlation between  $\tilde{\mathbf{U}}_{(T,R)}^a$  and  $P_R \in \mathbf{P}_R$  under the defined perfectly estimated LoS channel aimed to be exploited by using few-shot learning. Due to the uniqueness of each A2A trajectory channel  $\mathbf{h}_{R_i}$ , for each A2A link an  $\mathcal{S}$  exists where  $\mathbf{U}_{(T,R)_i}^a \subset \mathcal{S}$  and power constraints of  $\mathbf{U}_{(T,R)_i}^a$ , we

aim to solve this problem with a limited dataset. Accordingly, the L2L approach is resorted to employing domain generalization technique to overcome this barrier.

#### A. Meta-Learning

We utilize MAML with semantic segmentation network to estimate the  $\phi_R^{\psi, \theta}$  by using estimated  $P_R$  for a  $\mathbf{A}_R^a$  positioned UAV in space with  $\tilde{\mathbf{U}}_R^r$  direction. Thuswise, few-shot learning with  $N$ -way  $K$ -shot classification has been employed to utilize gradient descend. Here, a set of  $K$  exemplary data samples are employed for fine-tuning the model during the evaluation process, aimed at achieving the task of classifying  $N$  distinct classes.

In the search of finding the incident wave angles for more general Tx - Rx for UAV channels, the RSS distribution in  $\mathcal{S}$  such as  $p_S(P_R)$  is not only  $h_{R_i} \in \mathcal{S}, \forall i$  dependent, but also relies on  $\mathbf{R}_i^{ab}$  which has non-probabilistic distribution. Considering aforementioned antenna imperfections, analyzing such correlation between each  $\phi_R^{\psi, \theta} \in \Phi_R^{\psi, \theta}$  and  $p_S(P_R)$  is vastly difficult that any task based learning algorithms will eventually fail, as neither using an experimental dataset nor utilizing deeper layers of neural networks cannot help. In an L2L approach, meta-learning is able to train over the  $\mathcal{T}_i$  distribution to prioritize the learning convergence over the accuracy itself. Hence, instead of minimizing the loss function  $\mathcal{L}(f_{P_R}(\mathcal{D}))$  to optimize the model parameter, MAML lowers the misclassification error for the sake of fast adaptation of the learning over sampled  $\mathcal{T}_i$  distribution as following

$$\hat{Q}_{P_R} = \arg \min_{Q_{P_R}} \mathbb{E}_{\mathcal{T}_i \sim p(\mathcal{T})} \mathcal{L}_{\mathcal{T}}(f_{Q_{P_R}}). \quad (31)$$

In the L2L perspective, the behavior of different data subsets can be learned rather than the behavior of samples belonging to a dataset. The structure of the Eq. (31) will be explained broadly in Section IV-A3. It is acknowledged that, under strong assumptions such as having an ample amount of data and a precise understanding of the radio environment's behavior, a standalone CNN model might be more robust than meta-models. However, this assumption is often unrealistic. Meta-learning, on the other hand, offers a pragmatic approach, delivering reliable and realistic results for challenging problems in a manner that aligns with realistic and explainable AI principles.

1) *An Upper Bound for "n"*: In concern of convergence of this approach for the optimization of  $f_{Q_{P_R}}: \mathbf{P}_R \rightarrow \Phi_R^{\psi, \theta}$ , an upper probability bound for MAML can be shown with Hoeffding's inequality. The meta classifier  $f_{Q_{P_R}}$  defined on a finite domain of  $P_R$  variables and a random evaluation set of  $\mathcal{D}_{\text{eval}}$  classified by the  $f_{Q_{P_R}}$ . For each  $P_R$ ,  $\phi_R^{\psi, \theta}$  classification result with  $v_{(\Phi_R^{\psi, \theta}), i}, i \in \{1, \dots, n\}$ . With the knowledge of the true error rate of the classifier ( $\mathbb{E}(f_{Q_{P_R}})$ ), the success probability of classifier can be bounded as following:

$$\Pr\left(\sum_i v_{(\Phi_R^{\psi, \theta}), i} - \mathbb{E}[v_{(\Phi_R^{\psi, \theta}), i}] \geq \epsilon\right) \leq e^{-\frac{2\epsilon^2}{\sum_{i=1}^n (b_i - a_i)^2}}, \quad (32)$$

where the  $\epsilon \geq 0$  and  $a_i \leq P_{R_i} \leq b_i$  almost surely. In meta classification,  $v_{(\Phi_R^{\psi, \theta}), i}$  has been defined such that



$v_{(\Phi_R^{\psi,\theta}),i} = 0$  if  $f_{Q_{PR}}$  misclassify and  $v_{(\Phi_R^{\psi,\theta}),i} = 1$  in case classifier successes. Therefore, a Binomial random variable specified as  $a_i = 0$  and  $b_i = 1$  for all  $i$ . Thereby, the Hoeffding Bound is the following

$$\Pr\left(\sum_i v_{(\Phi_R^{\psi,\theta}),i} - \mathbb{E}[v_{(\Phi_R^{\psi,\theta})}] \geq \epsilon\right) \leq \exp\left(\frac{-2\epsilon^2}{n}\right). \quad (33)$$

Rearranging the Eq. (33) results with [53]

$$\begin{aligned} & \Pr\left(\frac{1}{n} \sum_{i=1}^n v_{(\Phi_R^{\psi,\theta}),i} - \mathbb{E}[v_{(\Phi_R^{\psi,\theta})}] \geq \epsilon\right) \leq \exp\left(-2\epsilon^2 n\right), \\ & = \Pr\left(\frac{1}{n} \sum_{i=1}^n v_{(\Phi_R^{\psi,\theta}),i} - \mathbb{E}[v_{(\Phi_R^{\psi,\theta})}] \geq \epsilon\right) \leq 2 \exp\left(-2\epsilon^2 n\right). \end{aligned} \quad (34)$$

Following the Eq. (34), the minimum number of samples required for a given confidence interval ( $\alpha_{\Phi_R}$ ) can be found. Therefore, the probability of accuracy error with ( $\mathbb{E}(f_{Q_{PR}}) \pm \epsilon$ ) confidence interval for the  $\mathcal{L}(f_{P_R}(\mathcal{D}))$  optimized using  $\{\mathcal{D}_{\text{train}}, \mathcal{D}_{\text{test}}\}$  is the following

$$\alpha_{\Phi_R} = \Pr(v_{(\Phi_R^{\psi,\theta})} \in (\mathbb{E}(f_{Q_{PR}}) - \epsilon, \mathbb{E}(f_{Q_{PR}}) + \epsilon)) \leq 2 \exp\left(-2\epsilon^2 n\right). \quad (35)$$

Finally, a tight bound for the  $n$  is the following

$$n \geq \frac{\log(2/\alpha_{\Phi_R})}{2\epsilon^2}, \alpha_{\Phi_R} \neq 0. \quad (36)$$

As a result, not only number of samples required can be estimated for a success threshold, but also the accountability of the model can be interpreted with the described bound.

2) *Task and Dataset Construction*: The task  $\mathcal{T}_i$  associated with  $\mathcal{D} = \{\mathcal{D}_{\text{train}}, \mathcal{D}_{\text{test}}\}$  where  $\mathcal{D}_{\text{train}}$  is the support set used during the learning and  $\mathcal{D}_{\text{test}}$  is the prediction set for training and testing. Each set contains feature vectors as  $P_R^{M \times N} \in \mathbf{P}_R$  as the set of corresponding incident wave angle  $(\Phi_R^{\psi,\theta})_{T_1 \times T_2}$  as where  $\mathbf{P}_R^{(m)} \subset (\Phi_R^{\psi(j),\theta(k)}) \subset \kappa_i, m \in \{1, \dots, M\}, j \in \{1, \dots, T_1\}, k \in \{1, \dots, T_2\}, i \in \{1, \dots, I\}$ . The following structure of  $\mathcal{D}$  allows to demonstrate the full potential of MAML as following

$$\begin{cases} \kappa_i \subset \mathcal{D}_{\text{train}}, & \text{if } i \text{ odd,} \\ \kappa_i \subset \mathcal{D}_{\text{test}}, & \text{otherwise,} \end{cases} \quad (37)$$

where  $(i, j, k, m) \in \mathbb{Z}$ . In this way, not only  $\mathcal{D}_{\text{train}}$  distinct from the  $\mathcal{D}_{\text{test}}$ , but also  $\mathcal{D}$  does not possess any other information such as SNR, CSI or  $\mathbf{F}_{T,R}$ . Note that, the antenna with  $\mathbf{F}_{T,R}((\psi^{(i)}, \theta^{(j)})) = \mathbf{F}_{T,R}((\psi^{(k \neq i)}, \theta^{(j)})), \forall i, j, k \in (0, \pi]$  allows constructing such a  $\Phi_R^{\psi(\cdot),\theta(k)}$  due to the fact that  $p(P_R | \psi_R, \theta_R) = p(P_R | \theta_R)$ . Therefore, utilizing  $\theta_R$  for the whole dataset drops the amount of used dataset from  $(T_1 \times T_2)$  to  $(1 \times T_2)$  without losing any information. Thus,  $N$ -way  $K$ -shot classification can be done with  $K \subset \mathcal{D}_{\text{train}}$  samples from different  $N$  classes. The defined dataset structure for the A2A link including antenna imperfections will be called 3D propagation model (3DPM) in the remaining part of the study.

Hereof,  $\mathcal{D}$  is generated by utilizing the impairment modeling discussed in Section III and the derived channel modeling presented in Section II. Therefore, probability distribution of

the far field constrained UAV distances with  $\phi^\theta$  orientation follows  $p_{\phi^\theta}(\phi^\theta | d)$  in Eq. (5). The joint antenna impairments distribution on  $E$  plane  $H$  plane is given in Eq. (27), and the directivity with Gaussian impairments are given in Eq. (29) and Eq. (30). Measured  $P_R$  is the noisy measurement under  $\mathbf{h}_{\ell,k}$  with an ideal antenna that contains  $\mathbb{U} \sim [0, 1]$  PLF. Since the  $\mathbb{E}(\mathbf{F}_R(\psi, \theta, \zeta)) = \mathbf{F}_R(\psi, \theta)$ , non-idealities in antenna are not included in the  $\mathcal{D}$ . The same assumption holds for unbiased Gaussian misalignment where  $\mathbb{E}(\delta_1) = \mathbb{E}(\delta_2) = 0$ . Recall that  $k$  way transmission indicates the duplex direction between the UAVs, so that A2A nodes can follow two way communication model [54]. However, in terms of meta training data, it does not require any additional data since the duality of the states. This means that, every state of  $\mathbf{U}_T$  to  $\mathbf{U}_R$  of  $k = 1$  has an equivalence when  $k = 2$ . For each  $\mathbf{p}_T^1 \xrightarrow{h} \mathbf{p}_R^2$ , a link such  $\mathbf{p}_T^2 \xrightarrow{h} \mathbf{p}_R^1$  exist. Every supervised classification task can be generalized as following [20]

$$\mathcal{T} = \{\mathcal{L}(P_R^{(1)}, \phi_R^{\theta,\psi,(1)}), p(P_R^{(1)}), p(P_R^{i+1} | P_R^i, \phi_R^{\theta,\psi,(i)}), 1\}. \quad (38)$$

In MAML,  $K$ -shot L2L model aimed to obtain a  $\mathcal{T}_i \sim p(\mathcal{T}), \forall i \in K$ , and then during the meta-training,  $f_{Q_{PR}}$  trains with the  $K$  samples by using the loss function  $\mathcal{L}_{\mathcal{T}_i}$  that will be defined later on. As mentioned before, meta-test results with enhanced tasks of  $\hat{\mathcal{T}}_i$ , concluding with the more optimized  $\hat{f}_{Q_{PR}}$  with  $\hat{Q}_{PR}$  parameters. 3DPM is a custom

---

**Algorithm 1** MAML Model Optimization for Incident Wave Angle Estimation

---

**Require:**  $p(\mathcal{T})$ : distribution over RSS measurement tasks for different sets of  $\mathbf{h}_{\ell,k}$  (3DPM dataset)

**Require:**  $\alpha$ : Inner learning rate,  $\beta$ : Meta step size

- 1: Randomly initialize  $Q_{PR}$
  - 2: **while** not done **do**
  - 3: Sample Meta-RSS batch measurements  $\mathcal{T}_i \sim p(\mathcal{T})$  in Eq. (38)
  - 4: **for all**  $\mathcal{T}_i$  **do**
  - 5: Sample  $K$  data points  $\mathcal{D} = \{P_R^{(j)}, \phi^{\theta(j),\psi(\cdot)}\}$  from  $\mathcal{T}_i$
  - 6: Evaluate  $\nabla_{Q_{PR}} \mathcal{L}_{\mathcal{T}_i}(f_{Q_{PR}})$  using  $\mathcal{D}$  and  $\mathcal{L}_{\mathcal{T}_i}$  in Eq. (40)
  - 7: Evaluation of tuned parameters with SGD:  $(Q_{PR})'_i = Q_{PR} - \alpha \nabla_{Q_{PR}} \mathcal{L}_{\mathcal{T}_i}(f_{Q_{PR}})$  in Eq. (41)
  - 8: Sample data points  $\mathcal{D}'_i = \{P_R^{(j)}, \phi^{\theta(j),\psi(\cdot)}\}$  from  $\mathcal{T}_i$  for the meta-update.
  - 9: **end for**
  - 10: Update  $Q_{PR} \leftarrow Q_{PR} - \beta \nabla_{Q_{PR}} \sum_{\mathcal{T}_i \sim p(\mathcal{T})} \mathcal{L}_{\mathcal{T}_i}(f_{Q_{PR}})$  using each  $\mathcal{D}'_i$  and  $\mathcal{L}_{\mathcal{T}_i}$  by Eq. (42) and Eq. (43) respectively.
  - 11: **end while**
- 

dataset for a supervised meta-learning algorithm generated with the discussed system model in Section II. It aims to convert a data learning process into task learning as efficiently as possible, so that the L2L approach can be performed. In the meta-learning, a training dataset  $\mathcal{D}_{\text{train}}$  is used for the training process and a small test set  $\mathcal{D}_{\text{test}}$  for adaptation to

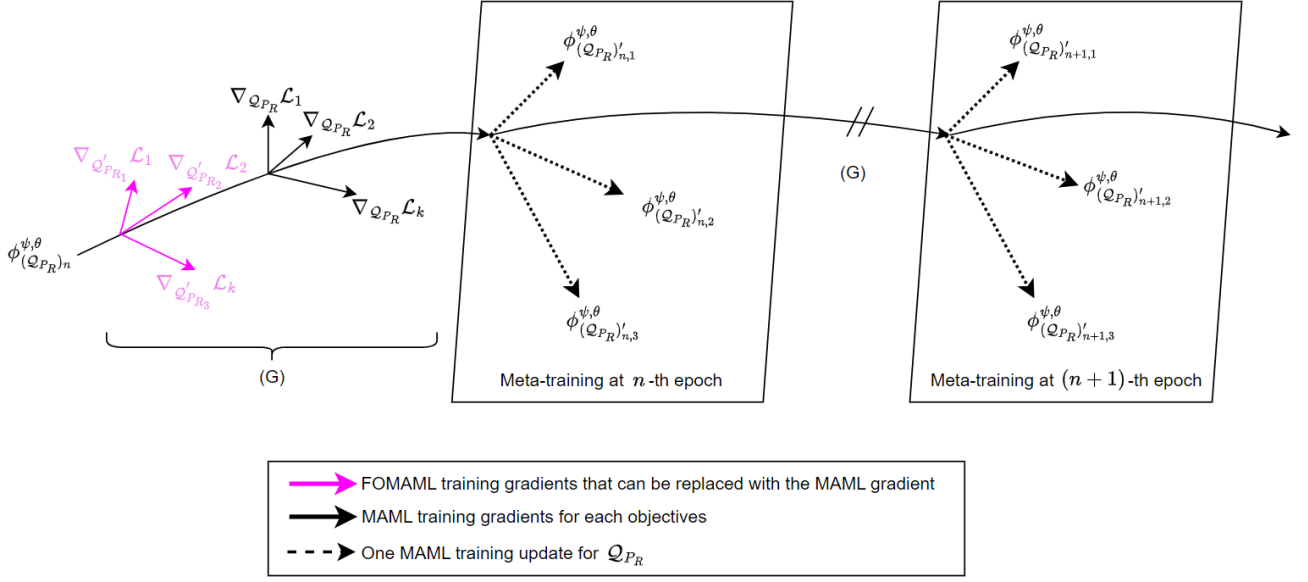


Figure 4.  $\phi_{(Q_{P_R})^n}^{\psi, \theta}$  adaptation for the optimal parameter vector for task  $i$  in each iteration.  $k$  objectives of sample beam angles for 3 inner steps has been shown for both MAML and FOMAML.

tune the parameters with each RSS received [20]. Domain generalization can be summarized in two steps:

- 1) Generate a set containing measured  $P_R$  for  $M$  different fading channel set by the  $K$ -factor.)
- 2) Separate the generated set into two parts with respect to fading channel  $K$ -factor. So that, different instances of similar tasks (which is the wave angle estimation) can be meta-trained during  $\mathcal{D}_{\text{test}}$  use.
- 3) Use  $n$  amount of task within  $\mathcal{D}_{\text{train}}$  and  $\mathcal{D}_{\text{test}}$  for the learning adaptation.

The first step ensures that the AI model is exposed to diverse datasets, which is preferable for any learning technique. The second and third step ensures that domain generalization is performed and  $n$  number of tasks learned and  $\mathcal{D}_{\text{test}}$  supports the  $Q_{P_R}$  for learning the already learned model.

3) *Meta-Optimization for Incident Wave Angle Estimation:* The mutual correlation for each  $\mathbf{P}_R \hat{=} \Phi_R^{\Psi, \Theta}$  optimization has been done by the tuning a model  $Q_{P_R}$  parameter in the negative direction of the gradient as following

$$(Q_{P_R})'_i = Q_{P_R} - \alpha \nabla_{Q_{P_R}} \mathcal{L}_{\mathcal{T}_i}^{(0)}(f_{Q_{P_R}}), \quad (39)$$

where  $f_{Q_{P_R}}$  is the model with parameters  $Q_{P_R}$ ,  $\mathcal{T}_i$  is the task of optimization by utilizing the datasets  $\{\mathcal{D}_{\text{train}}^{(i)}, \mathcal{D}_{\text{test}}^{(i)}\}$  and  $\mathcal{L}(\cdot)^{(i)}$  is the cross entropy loss function of  $i$ -th data batch for the supervised classification task  $\mathcal{T}_i \sim p(\mathcal{T})$  defined as following

$$\begin{aligned} \mathcal{L}_{\mathcal{T}_i}(f_{Q_{P_R}}) = & \sum_{\mathbf{P}_R^{(j)}, \Phi^{\Psi, \Theta(j)} \sim \mathcal{T}_i} \Phi^{\Psi, \Theta(j)} \log f_{Q_{P_R}}(\mathbf{P}_R^{(j)}) + \dots \\ & + (1 - \Phi^{\Psi, \Theta(j)}) \log(1 - f_{Q_{P_R}}(\mathbf{P}_R^{(j)})), \quad (40) \end{aligned}$$

where the loss function input/output pairs are denoted as  $P_R^{M \times N} \in \mathbf{P}_R$  and  $\phi^{\psi, \theta} \in \Phi^{\Psi, \Theta}$  respectively. In such a scenario

with initial parameter of  $(Q_{P_R})^\circ$  is selected, the inner gradient steps are following

$$\begin{aligned} (Q_{P_R})_0 &= (Q_{P_R})^\circ \\ (Q_{P_R})_1 &= (Q_{P_R})_0 - \alpha \nabla_{Q_{P_R}} \mathcal{L}_{\mathcal{T}_i}^{(0)}((Q_{P_R})_0) \\ (Q_{P_R})_2 &= (Q_{P_R})_1 - \alpha \nabla_{Q_{P_R}} \mathcal{L}_{\mathcal{T}_i}^{(0)}((Q_{P_R})_1) \\ &\vdots \\ (Q_{P_R})_k &= (Q_{P_R})_{k-1} - \alpha \nabla_{Q_{P_R}} \mathcal{L}_{\mathcal{T}_i}^{(0)}((Q_{P_R})_{k-1}). \end{aligned} \quad (41)$$

The naturalization of meta-tasks to evaluate  $\hat{Q}_{P_R}$  by recursive iteration until to get an optimum  $\phi_R^{\psi, \theta}$  steps has been shown as

$$\begin{aligned} \hat{Q}_{P_R} &= \arg \min_{Q_{P_R}} \sum_{\mathcal{T}_i \sim p(\mathcal{T})} \mathcal{L}_{\mathcal{T}_i}^{(1)}(f_{(Q_{P_R})'_i}), \\ &= \arg \min_{Q_{P_R}} \sum_{\mathcal{T}_i \sim p(\mathcal{T})} \mathcal{L}_{\mathcal{T}_i}^{(1)}(f_{Q_{P_R} - \alpha \nabla_{Q_{P_R}} \mathcal{L}_{\mathcal{T}_i}^{(0)}(f_{Q_{P_R}})}). \end{aligned} \quad (42)$$

Hence, the update of  $Q_{P_R}$  within the same task  $\mathcal{T}$  is

$$Q_{P_R} \leftarrow_{\mathcal{T}_i} Q_{P_R} - \beta \nabla_{Q_{P_R}} \sum_{\mathcal{T}_i \sim p(\mathcal{T})} \mathcal{L}^{(1)}(f_{Q_{P_R} - \alpha \nabla_{Q_{P_R}} \mathcal{L}^{(0)}(f_{Q_{P_R}})}). \quad (43)$$

As can be seen in Eq. (41) and Algorithm 1, SGD performs the second derivation on  $Q_{P_R}$  in the evaluation of  $(Q_{P_R})'_i$ . As a significant note, the  $(Q_{P_R})'$  can be achieved with just a few steps in Eq. (41), instead of calculating nearly 50 inner gradient steps as in [34] where the gradient vanishes and last layer does not update any weights. Using only the final gradient  $k$  is an alternative approach for high dimensional calculations where the second-order derivatives are overcostly for trivial profit.

A meta-model can be further adapted to several fading channels. Here, we define the tasks in terms of RSS values

under different fading channels. In this regard, the following two steps present the whole multi task meta-learning scheme:

$$\hat{Q}_{P_R} = \arg \min_{Q_{P_R}} \sum_{i=1}^n \mathcal{L}(\varphi_i, \mathcal{D}_{\text{test},i}) \quad (44)$$

and

$$\varphi_i = f_{Q_{P_R}}(\mathcal{D}_{\text{train},i}) \quad (45)$$

where  $\mathcal{D}_{\text{train}}$  contains  $\mathbf{h}_{\ell,k}$ ,  $\mathcal{D}_{\text{test}}$  contains “few” amount of  $\exists n : \mathbf{h}_{\ell,k}$ . In contrast to generic supervised learning, meta-learning minimizes the sum of  $n$  task of the loss function on the  $\mathcal{D}_{\text{test},i}$  with respect to  $\varphi_i$ . Thus,  $n$  amount of tasks exist and each task  $\tau_i$  owns  $\mathcal{D}_{\text{train},i}$  and  $\mathcal{D}_{\text{test},i}$ . Here,  $f_Q$  is a neural network (which is a CNN in our case) and  $\mathcal{D}_{\text{train},i}$  generates the  $\varphi_i$  which can be used for  $\mathcal{D}_{\text{test},i}$  within the same task that minimizes the loss. In this regard, the learning of RSS for  $n$  amount of different fading channels is performed during the testing step for each task. Learning the generalized tasks in contrast to learning the dataset itself improves the adaptability of the model further. Thus, an idea over an unknown fading channel can be obtained.

### B. A Faster MAML Technique: FOMAML

One alternative L2L variation to MAML algorithm is the FOMAML which bypasses the second derivative in the outer SGD. It has been shown that [55] FOMAML is not only more feasible to implement, but also it can generalize as closely as the original MAML in some situations where the dataset contains out-of-sample data points, as also known as outliers. In such cases, FOMAML with low order gradient calculation would perform even better.

Outer loop update of the  $Q_{P_R}$  in Algorithm 1- step 10 for  $k$  inner gradient step is simplified as taking the last inner gradient step ( $k$ ) into consideration in Algorithm 1- step 7. Thus, update equivalent disposes the  $\nabla_{Q_{P_R}}$  products within the inner step. Recalling that  $\mathcal{L}$  is a differentiable function, Algorithm 1- step 10 simply calculates the gradient of outer gradient  $Q_{P_R}$  as following

$$\begin{aligned} Q_{P_R} &\leftarrow Q_{P_R} - \beta \nabla_{Q_{P_R}} \sum_{\mathcal{T}_i \sim \mathcal{P}(\mathcal{T})} \mathcal{L}_{\mathcal{T}_i}(f_{Q_{P_R}}) \\ &\leftarrow Q_{P_R} - \beta \sum_{\mathcal{T}_i \sim \mathcal{P}(\mathcal{T})} \nabla_{Q_{P_R}} \mathcal{L}_{\mathcal{T}_i}(f_{Q_{P_R}}) \\ &\leftarrow Q_{P_R} - \beta \sum_{\mathcal{T}_i \sim \mathcal{P}(\mathcal{T})} (\nabla_{Q_{P_R}} Q'_{P_{R_i}}) \nabla_{Q'_{P_{R_i}}} \mathcal{L}_{\mathcal{T}_i}(f_{Q'_{P_{R_i}}}) \end{aligned} \quad (46)$$

Using the inner gradient equivalent of  $(Q_{P_R})'_i = Q_{P_R} - \alpha \nabla_{Q_{P_R}} \mathcal{L}_{\mathcal{T}_i}(f_{Q_{P_R}})$  of Eq. (39) on Eq. (46) finalizes the objective update analysis for MAML as in

$$Q_{P_R} \leftarrow Q_{P_R} - \beta \sum_{\mathcal{T}_i \sim \mathcal{P}(\mathcal{T})} \underbrace{(\mathbf{I} - \alpha \nabla_{Q_{P_R}}^2 \mathcal{L}_{\mathcal{T}_i}(f_{Q_{P_R}})) \nabla_{Q'_{P_{R_i}}} \mathcal{L}_{\mathcal{T}_i}(f_{Q'_{P_{R_i}}})}_{\text{Requires Hessian}}. \quad (47)$$

Thus, the explicit expression of optimizer gradient given in Eq. (43) is obtained in Eq. (47). FOMAML algorithm simply ignores the Hessian term and takes the indicated term into

account as  $\mathbf{I}$  for the current sample batch. This technique can be replaced with MAML as illustrated in Figure 4.

### C. Incident Wave Azimuth Angle Estimation

The solution for  $\phi_R^\psi$  can be obtained by exploiting the invariant null zones of the antenna and the estimated elevation angle of the incident wave. Beam scanning, steering and eigendecomposition of the received signal via multiple signal identification classification (MUSIC) are some of the widely adopted techniques for achieving  $\phi_R^\psi$  estimation objective. Without needing any CSI or MPC information,  $\phi_R^\psi$  can be found directly by the  $P_R$  and estimated  $\tilde{\phi}_R^\theta$  by few-shot learning. Therefore, for this part of the study,  $\phi_R^\psi$  can be found by rotating the antenna pattern for each  $\phi_R^\theta$  until to find the minimum RSS level, as will be indicated as the  $\phi_R^\psi$ . With the assumption that  $\tilde{\phi}_R^\theta$  is correct, a similar approach in [5],  $\tilde{\phi}_R^\psi$  solution is possible in  $\tilde{\phi}_R^\theta$  direction. Holding the previous assumption that Rx antenna has the same  $\mathbf{A}_R^r$  with its UAV, this rotation needs to be done with the kinematic motion of the  $\mathbf{U}_R^r$ . First, locate the antenna along the axis through the elevation angle by either<sup>2</sup> roll or pitch orientation as follows

$$\mathbf{U}_{\text{steer}}^\theta = \mathbf{R}_z(\mathbf{I})\mathbf{R}_y(\Theta_2(\tilde{\psi}^\theta))\mathbf{R}_x(\mathbf{I})\mathbf{U}_b, \quad (48)$$

where the  $\tilde{\psi}^\theta$  is the rotation angle through the estimated  $\theta$  by the MAML. Beam steering with  $l \in \mathbf{I}$  steps are defined for each beam samples as following

$$P_R^{\theta,\psi(l)} = \begin{cases} \mathbf{R}_z(\Theta_1(l))\mathbf{R}_y(\mathbf{I})\mathbf{R}_x(\mathbf{I})\mathbf{U}_{\text{steer}}^\theta, & \text{if } \hat{\mathbf{u}}_0 \parallel \hat{e}_z \\ \mathbf{R}_z(\mathbf{I})\mathbf{R}_y(\Theta_2(l))\mathbf{R}_x(\mathbf{I})\mathbf{U}_{\text{steer}}^\theta, & \text{if } \hat{\mathbf{u}}_0 \parallel \hat{e}_y \\ \mathbf{R}_z(\mathbf{I})\mathbf{R}_y(\mathbf{I})\mathbf{R}_x(\Theta_3(l))\mathbf{U}_{\text{steer}}^\theta, & \text{if } \hat{\mathbf{u}}_0 \parallel \hat{e}_x \end{cases} \quad (49)$$

Sweeping the beams so that the optimum  $\phi^\psi$  for the corresponding  $\phi^\theta$  will be the  $l$ -th beam sample that gets the minimum  $P_R$ , ideally zero.

$$\tilde{\phi}^\psi = \arg \min_{l \in \mathbf{I}} P_R^{\theta,\psi(l)} \quad (50)$$

This concludes the both azimuth and elevation angle estimations of an incident wave.

---

#### Algorithm 2 CNN Model Optimization for Incident Wave Angle Estimation

---

**Require:**  $\mathcal{T}$ : RSS measurement tasks

**Require:** Optimizer learning rate ( $\alpha$ ), Batch size ( $b$ )

- 1: Randomly initialize  $Q_{P_R}$
  - 2: Randomly initialize task selection with  $\mathcal{T}_i \sim \mathcal{T}$
  - 3: **for all**  $\mathcal{T}_i$  **do**
  - 4: Construction of training batch  $\mathcal{B}_i^b$  with  $\mathcal{D} = \{P_R^{(j)}, \phi^{\theta(j),\psi(\cdot)}\}$  from  $\mathcal{T}_i$
  - 5: Evaluate  $\nabla_{Q_{P_R}} \mathcal{L}_{\mathcal{T}_i}(f_{Q_{P_R}})$  using  $\mathcal{B}_i^b$
  - 6: Evaluation of tuned parameters with SGD:  $Q'_{P_{R_i}} = Q_{P_R} - \alpha \nabla_{Q_{P_R}} \mathcal{L}_{\mathcal{T}_i}(f_{Q_{P_R}})$
  - 7: **end for**
- 

<sup>2</sup>The difference in roll and pitch initials corresponds to different  $\psi$  angles, therefore an arbitrary choice does not affect the  $\psi$  estimation since steering covers each of beam samples.

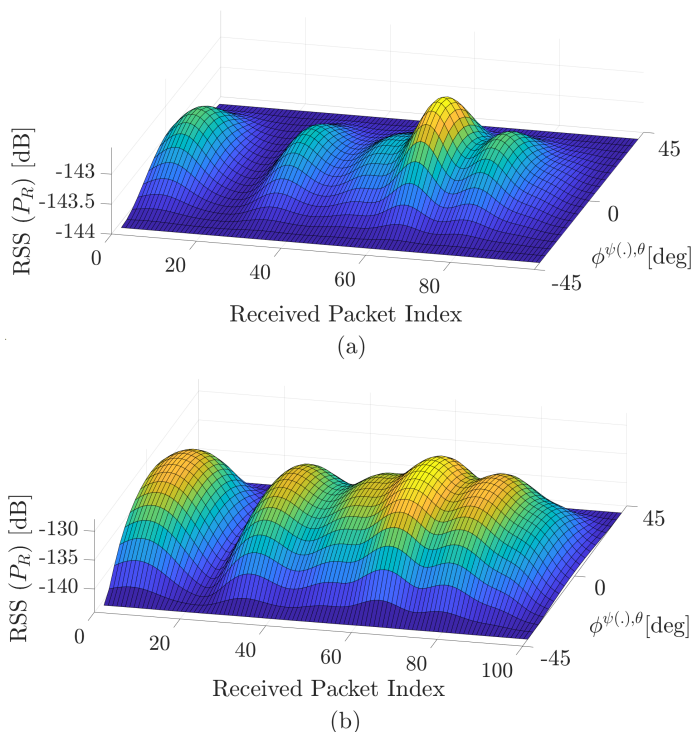


Figure 5. Impact of incident elevation angle of the signal on RSS level with  $P_T = 10$  dB (a) and  $P_T = 30$  dB (b).

## V. NUMERICAL RESULTS

In this section, the numerical evaluations of the proposed methods have been presented and discussed. The corresponding model parameters are placed in Table I. Firstly, the simulation environments and performance metrics have been explained. Then, the impact of a non-ideal antenna radiation pattern on the fading channel has been numerically evaluated. In continuation, explained MAML and FOMAML algorithms have been implemented for the estimation of  $\phi_R^{\psi, \theta}$ . Lastly, a well-known CNN model has been generated for benchmark tests and comparison tools. Due to use of model-agnostic approach, any model can be utilized along with the meta-optimization. For instance, it can be a support vector machine, decision tree, or a neural network (which is a simple CNN in our approach). That's why we utilize the exact same CNN model for a comparison, highlighting the significance of MAML improvement on the simple task optimization.

Similarly, a feed-forward DenseNet is utilized for the same objective with using the same dataset. The DenseNet – BC architecture with  $k = 12$  growth rate and  $L = 100$  layers scheme is summarized in Table III. It uses bottleneck layers in each Dense Block for parameter reduction. While the same optimizer momentum rate and loss function structure are utilized for supervised classification, specific emphasis is placed on highlighting the distinctive parameters unique to the DenseNet architecture. The model contains 3 dense block which contains 96 bottleneck layers where each layer takes all preceding feature maps as input. The drop rate is 0.2, and total of contains 2 transition layers between the dense blocks. The model progressively reduces the spatial dimensions of feature

maps while increasing the number of channels, resulting in a compact representation suitable for beam classification. Therefore, the feature maps are compressed with the order of compression factor  $C^* = 0.5$  within each transition layers. After the dense blocks, a global average pooling layer followed by softmax activation as a logistic classifier, just as in MAML.

$M = 20$  and  $N = 100$  sized RSS matrix as the set of  $\mathcal{D}$  has been used to perform joint training and testing process. In previously defined 3DPM dataset, it has been set to  $T_2 = 20$  instances of 180 RSS samples that corresponds to each  $\Phi_R^{\Theta(i)}$  for each  $i \in [-\frac{\pi}{2}, \frac{\pi}{2}]$  from  $\kappa = \{0, 1, 2, \dots, 30\}$  channels. One reason for using Rician fading with both high and low  $\kappa$  is to create a  $\mathcal{D}$  such that a base meta-model that utilizes  $\mathcal{D}_{\text{train}} \subset \mathcal{D}$  can also excel in untrained and unseen tasks with fine-tuning parameters with  $\mathcal{D}_{\text{test}} \subset \mathcal{D}$ . Therefore, we turn the objective from Rician fading channel learning into a fading channel learning. Diversity of prior distributions across the tasks is provided with channel fading [56] as in Eq. (41) for  $\mathcal{D}_{\text{train}}$  and  $\mathcal{D}_{\text{test}}$  subsets [57]. There is no further augmentation and modification on the dataset. Throughout the numerical evaluation of the receiver, it has been assumed that CSI at the receiver is known. The different  $K$  and  $N$  scenarios of meta-classification have been tried within the same dataset. The impact of  $N$ -way classification has been evaluated with  $N = \{6, 8, 10\}$  while the  $K$ -shot effect has been compared within the same  $N$ -way classification. In these concepts, the evaluation of meta-classification steps follows the Algorithm 1 step 4 – 9 as follows:

- 1) Select random  $N$  classes from  $\mathcal{D}_{\text{eval}}$ .
- 2) Pick  $K$  instances for each class to fit the model.
- 3) Performing the evaluation for different instances within the same class.

Hence, the evaluation of meta-model performs SGD over  $K$  samples to tune  $Q_{P_R}$  parameters, as the underlying principle of L2L that learning over the learned model. The evaluation dataset  $\mathcal{D}_{\text{eval}}$  contains  $P_R^{1000 \times 100} \in \mathbf{P}_{R, \text{eval}}$  generated on the 3DPM defined in Table IV by the same method has been used to generate  $\mathcal{D}$  with  $M = 1000$  in Section (IV-A2). The architecture model consists of 4 of convolution filter blocks with each containing 64 filters with  $3 \times 3$  kernel, a batch normalization, followed by a ReLU function and  $2 \times 2$  max-pooling respectively. Each  $P_R^{1 \times 100}$  sample create  $\mathbf{P}_R$  and last layer activation function SoftMax returns an array of probability score as usual. Some key parameters of the MAML have been shown in Table IV. The FOMAML follows the exact same process with the induced outer gradient version as explained previously.

### A. Performance Metrics and Simulation Environment

Accuracy is one of the metrics in evaluation of meta-classification defined as following

$$\text{Accuracy} = \frac{\sum_{\mathcal{D}_{\text{test}}} \mathbb{1}\{\tilde{\mathbf{c}}_R^{\phi, \theta} = \mathbf{c}_R^{\phi, \theta}\}}{M \times N} \quad (51)$$

where the  $\tilde{\mathbf{c}}_R^{\phi, \theta}$  is the estimated beam sample and  $\mathbf{c}_R^{\phi, \theta}$  is the ground truth beam sample. The very same accuracy

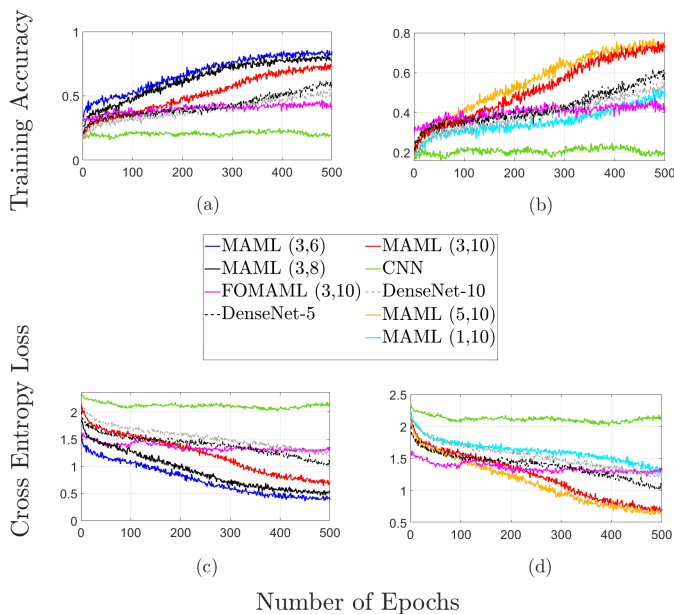


Figure 6. Learning curves comparison for different MAML( $K,N$ ), FOMAML( $K,N$ ), CNN and DenseNet- $N$  estimator models with the same iteration number.

definition is also valid for the evaluation with its dataset will be discussed.

Apart from the beam classification accuracy, the direct angle estimation errors can be bounded as following: Angle estimation error ( $\epsilon_\phi = \phi - \bar{\phi}$ ) can be defined in two different categories:

- 1) Angle estimation error in case of correct beam prediction, denoted as  $\epsilon_\phi^1$
- 2) Angle estimation error in case of faulty beam prediction, denoted as  $\epsilon_\phi^0$

We note that  $\epsilon_\phi^1 \leq \frac{\pi}{N} \leq \epsilon_\phi^0$  and  $\epsilon_\phi^1 \sim \mathcal{U}(0, \frac{\pi}{N})$  and  $\epsilon_\phi^0 \in (\frac{\pi}{N}, \pi]$ . Note that the resolution on angle estimation error can go down to 0, as  $N$  goes to infinity. In this case, if the classification is correct, the  $\phi^{\psi,\theta}$  is correct with  $\epsilon_\phi^1 = 0$ . However, as we also discuss in the original manuscript, this is only possible with a classification accuracy trade-off.

As indicated earlier, the classification error can be skeptical in Meta-RSS, therefore Hoeffding's PoC bounds the success point probability of the generated models as derived in Section IV-A1.

$$\text{PoC} = \exp(-2\epsilon^2 n) \quad (52)$$

$$\text{Point Probability} = \Pr\left(\frac{1}{n} \sum_{i=1}^n \nu_{(\Phi_R^{\psi,\theta}),i} - \mathbb{E}[\nu_{(\Phi_R^{\psi,\theta})}] \geq \epsilon\right) \quad (53)$$

## B. Evaluation of the Results

The impact of the antenna pattern has been illustrated in Figure 5. The highlight of this study emphasized with the  $P_R^{1 \times 100}$  measurements over  $\tilde{\mathbf{U}}_R^r$  having an ideal antenna on  $xy$ -plane with  $\phi^{\psi(\cdot),\theta} \in [-\pi/4, +\pi/4]$  incident elevation angle

Table III. DenseNet Architecture

Layers	DenseNet	Output Size
Convolution	$3 \times 3$	$32 \times 32$
Dense Block 1	$\begin{bmatrix} 1 \times 1 \\ 3 \times 3 \end{bmatrix} \times 24$	$32 \times 32$
Transition Layer 1	$1 \times 1$ conv $2 \times 2$ avg pool	$32 \times 32$ $16 \times 16$
Dense Block 2	$\begin{bmatrix} 1 \times 1 \\ 3 \times 3 \end{bmatrix} \times 108$	$16 \times 16$
Transition Layer 2	$1 \times 1$ conv $2 \times 2$ avg pool	$16 \times 16$ $8 \times 8$
Dense Block 3	$\begin{bmatrix} 1 \times 1 \\ 3 \times 3 \end{bmatrix} \times 150$	$8 \times 8$
Classification	global avg. pool softmax	$1 \times 1$ 10

at the receiver. The increment in  $P_T$  for  $\mathbf{U}_T^r$  demonstrates a widespread influence on RSS. However, the presence of a multiplicative incident wave angle term within the path loss restricts this influence regardless of the prevailing channel state. In the same figure, it can be seen that increment in  $P_T$  becomes negligible for near-null pattern zones, showing the significance of the 3DPM involving antenna characteristics where the incident wave angle information can mitigate this  $P_T$  bottleneck for the link.

The loss and training accuracy curves of the generated models can be seen in Figure 6, which underscores the importance of MAML's enhancements in optimizing simple tasks, demonstrating successful generalization across  $\mathcal{T}_i$  and transforming the basic CNN model into a robust and adaptive model. However, it is observed that, both DenseNet-5 and DenseNet-10 accomplished to capture features on 3DPM within the limited iteration allowance. The NVIDIA Tesla-T4 has been utilized to perform learning algorithms with CUDA 12.0 in 6 hours. PyTorch framework has been used to perform few-shot learning algorithm to joint training-testing process. In FOMAML, the duration of training drops from 6 to 2 hours and a half hour with fast training convergence. The comparison of different  $N$  with the same  $K = 3$  can be seen in Figure 6(a) and (c), while the comparison of different  $K$  with the same  $N = 10$  is shown in Figure 6(b) and (d). With the 500 epochs iteration, the models have reached their achievable performances where they get bottlenecked by the number of channels and dataset size, except MAML(5,10). It depicts that increasing  $N$  requires more iteration to converge as can be seen on MAML(5,10) case. Additionally, the simulations exclusively focus on examining the  $\mathbf{U}_R^r$  under rotational impact for the sake of simplicity. This deliberate choice positions the  $\mathbf{U}_R^r$  as the controlled variable, while the  $\mathbf{U}_T^r$  serves as a background to compare the impact of the receiver UAV state.

The  $\phi_R^\theta$  estimation accuracy performance of different methods have been shown in Figure 7. The initial observation reveals that the performance of the CNN classifier does not portray improvement as the SNR increases. The CNN, which estimates the beam samples with a high variance of approximately 0.16, demonstrates overfitting and exhibits weakness

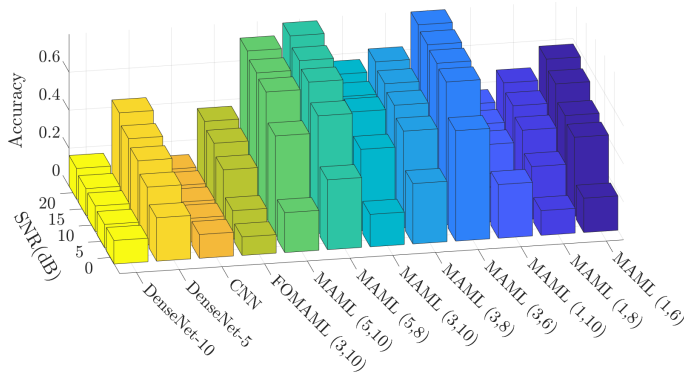


Figure 7. Evaluation of elevation classification with CNN, DenseNet- $N$ , MAML( $K,N$ ) and FOMAML( $K,N$ ) models for 0 – 20 dB SNR range.

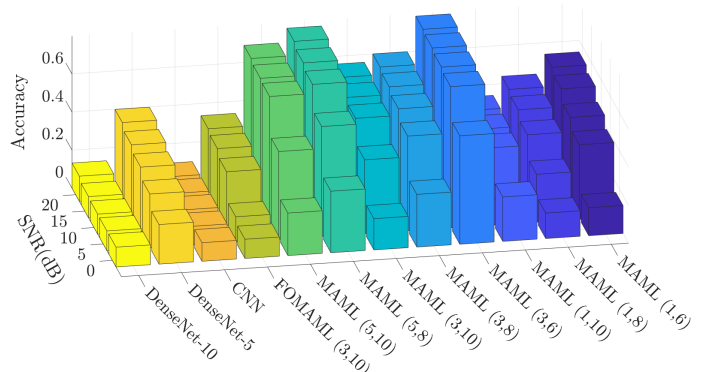


Figure 8. Evaluation of azimuth classification with CNN, DenseNet- $N$ , MAML( $K,N$ ) and FOMAML( $K,N$ ) models for 0 – 20 dB SNR range.

compared to all other configurations.

Despite its learning capabilities, the evaluation of DenseNet does not accurately reflect its learning accuracy, as anticipated. Note that this outcome arises not only because  $\mathcal{D}_{\text{eval}}$  includes unseen  $P_R$  for  $\phi^{\theta,\psi}$ , but also because the objective itself is unseen, given that the evaluation fading channel is not part of  $\mathcal{D}_{\text{train}}$ . However, unlike CNN, both DenseNet architectures exhibit enhancements as the SNR level increases. For instance, DenseNet – 5 demonstrates a notable improvement, with its accuracy rising from 22.8% at 0 dB to 43.9% at 20 dB. However, this enhancement is less pronounced in DenseNet – 10. Conversely, all other models consistently enhance their accuracy above the 0 dB threshold. Notably, reducing the  $N$  or increasing the  $K$  consistently enhances the performance. After reaching a 15 dB level, all scenarios encounter an error floor in different levels, with the MAML(3,6) configuration achieving a maximum accuracy performance of 0.74. The MAML(1,10) experiment initially resembles the behavior of the CNN at 0 dB but reaches to maximum accuracy performance of 0.3 eventually. In general, the one-shot experiments demonstrate relative success but rather poor performance compared to the cases with  $K = 3$  and  $K = 5$ . Table V presents the classifier accuracy within the same SNR level for different model configurations.

Later on, the  $\phi_R^{\psi}$  estimation accuracy for different cases has been evaluated in Figure 8. Similarly, MAML and FOMAML outperform both state-of-the-art CNN and DenseNet models, not only in terms of accuracy but also in the convergence of

the algorithms. It has been observed that the first step elevation estimation correlates with the azimuth estimation. Numerical observations indicate that while CNN exhibits a learning curve, it demonstrates suboptimal classification performance in evaluation tests. Moreover, DenseNet – 5 shows similar trend with elevation accuracy. However, DenseNet – 10 performs as well as CNN and it loses the demonstrated improvement depending on the SNR.

For comparison with previous researches of [46], [47] with similar purposes, our proposed method utilizes the omnidirectivity within  $\phi^{\theta} \in (0, 2\pi]$  and  $\phi^{\psi} \in (0, \pi]$ , therefore only estimation loss appear through the nulls where  $\theta = \{-\pi/2, \pi/2\}$ . Understandably, the accuracy through the null regions lowers down due to lowered SNR. At this point, the advantage of A2A link can appear where the UAVs are free to restrict their orientation and position to meet the controllability and observability conditions. Nevertheless, note that [46], [47] don't take a channel into account (only noise), and therefore the accuracy level is much better than our models, yet not realistic. On the downside, both studies do not require prior information for data driven method as this research method does. For an empirical study, a recent study [58] is an experimental study that makes use of RSS and channel state information for positioning, and states the new trainable model requirement for new environment in the experiments, while the proposed model on this study has succeeded within a single meta-model. In line with the previously discussed meta-model configuration in Section IV-A-3, a beam prediction application with a comparable MAML is conducted as presented in [34]. It is noteworthy that the accuracy reported in [34] falls below 60%, whereas our study achieves a higher accuracy of 75.8%.

Table IV. Few-shot learning and 3DPM parameters

Meta-Parameters	Value	3D Propagation Model Parameters	Value
Number of classes ( $N$ )	{6,8,10}	$\kappa$	12
Number of shots ( $K$ )	{1,3,5}	PLF	$\mathbf{U} \sim [0, 0.5]$
Inner train step ( $k$ )	1,3	$\mu_{\zeta}$	0
Inner learning rate ( $\alpha$ )	0.4	$\Sigma_{\zeta}$	0.2 $\mathbf{I}$
Meta-RSS Batch size	10	$\delta_{T1}, \delta_{R1}$ [deg]	0.05, 0.05
Number of Epochs	500	SNR [dB]	0-30 dB
Task (outer) learning rate	0.001	$d_x, d_y, d_z$ [m]	{100, 10, 5}
Meta step size ( $\beta$ )	0.999	$\mathbf{U}_T^a, \mathbf{U}_R^a$	[0, 0, 1] $^T$

The performance evaluation revealed that while the FOMAML technique exhibited faster learning capabilities, it also demonstrated slightly lower accuracy than MAML, as expected. The FOMAML accuracy with  $N = 10$ ,  $K = 3$  is limited with 0.39 in high SNR whereas the MAML can reach up to 0.57 accuracy with the same classification scheme. Hence, it can be inferred that the exclusion of the second derivative results in a loss of information in the learning process using 3DPM dataset, in contrast to the general ac-

ceptance that FOMAML accuracy is nearly same as MAML. On the other hand, FOMAML is still applicable for its low-cost efficiency since it is able to classify the limited data while CNN cannot. On top of this, FOMAML azimuth accuracy is directly proportional to the FOMAML elevation accuracy, as MAML technique does.

On the Figure 9, hereusticly, PoC bound indicates the performance difference between MAML and FOMAML where  $n > 45$  approaches for point probability in  $\epsilon = 0.25$  and  $n > 500$  for point probability in  $\epsilon = 0.05$ . Point probabilities show that MAML is more robust in strict classification than FOMAML in low  $\epsilon$  thresholds at the same  $n$ . Figure 9(a) and 9(b) depicts the  $\epsilon = 0.25$  tolerance cases for MAML and FOMAML. It can be seen that, with such a high tolerance level, the amount of sample required is nearly similar, while MAML convergence slightly better at the same  $n$ , as such highlighted interval of 45 – 50. This convergence gap is even wider in the lower tolerance threshold of  $\epsilon = 0.05$  as can be seen in Figure 9(c) and Figure 9(d). Comparing these with the first two subfigures in a and b, the required  $n$  is substantially increased and the convergence points are not as close. On this basis, it can be concluded that for 10 times more samples, the error tolerance for MAML(3,10), FOMAML(3,10) applications can be reduced from 0.25 to 0.05. Similarly, for more sensitive applications MAML offers a much safer option, while for low tolerance applications FOMAML can also be viable.

In terms of the impact of 3DPM, it has been noted that  $d_x, d_y, d_z$  related  $\delta_{T1}$  and  $\delta_{R1}$  results with coherency problem between the dataset and the model as the misalignment. Nevertheless, this drawback can be suppressed by lowering the  $N$ , the beam sampled classes, in return for accuracy performance. It has been observed that the accuracy levels go down to 30% in the Rayleigh fading case evaluation environment. This performance is notably lower compared to LoS scenarios. In NLoS case, the RSS presents low dimension information to separate such a complex scenario, this environment challenges the purpose we try to accomplish.

A significant contribution of the proposed angle estimation method is, that the UAVs don't require mutual information of

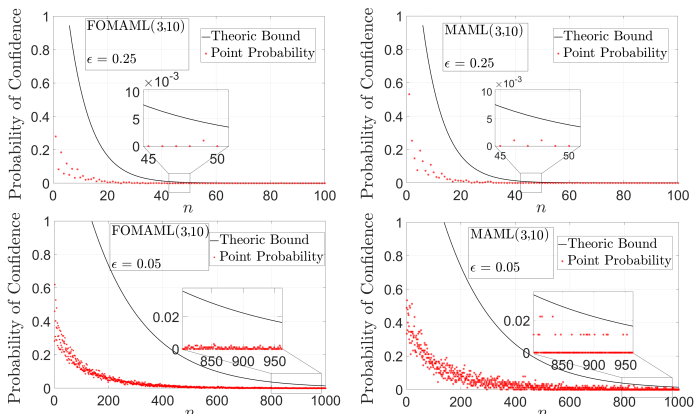


Figure 9. Probability of confidence bounds for both MAML and FOMAML with  $\epsilon = 0.25$  and  $\epsilon = 0.05$ .

Table V. Accuracy performance of the models in 10dB

Method		$N = 6$	$N = 8$	$N = 10$
MAML	$K = 1$	0.443	0.364	0.313
	$K = 3$	0.754	0.547	0.515
	$K = 5$	-	0.700	0.649
FOMAML	$K = 3$	-	-	0.272
CNN	-	0.16 $\pm$ 0.12		
DenseNet	-	0.23 $\pm$ 0.12		

each other (or require state estimation). Meta-model estimator requires the use of only a data driven model and a real time RSS. Note that the necessary information may be required as the system deviates from the ideal state. During the real time RSS processing, the age of information of RSS is directly related to the meta-model performance. Similarly, a power optimization over the network also negative impact over the proposed estimator for the designed 3DPM dataset. As the number of effects on the system model is increased, our model becomes gradually unstable, just as any machine learning approaches. On the upside, with more prior information, the system can be even more generalized.

The limitations of the proposed model's accuracy are mainly the due to the selection of limited sized dataset. In the realm of AI's progression towards leveraging small datasets, we aim to showcase the efficacy of meta-learning intentionally designed for limited datasets. Meta-learning proves to be an ideal tool for this purpose, leveraging subdatasets instead of the data itself. Emphasizing that the quality and diversity of the data hold greater significance than sheer volume, we acknowledge that dealing with limited data poses challenges such as overfitting, particularly evident in the case of CNN. Interestingly, employing DenseNet within the framework of MAML rather than a simple CNN presents a promising avenue for enhancing the precision of incident wave angle estimation, albeit at the cost of increased computational complexity. Regarding FOMAML, its influence manifests diversely across various types of studies. The authors on [59] demonstrate that experiments on MiniImageNet and Omniglot reveal that FOMAML performs almost as well as MAML. However, this outcome is not universally guaranteed, which leads to alternative models such as Reptile [55]. In our model, we observe the rapid convergence of FOMAML, consistent with its claims. However, it's worth noting that the significance of the second gradient loss for the given task is substantial, leading to a noticeable reduction in accuracy.

## VI. RECOMMENDED RESEARCH DIRECTIONS

Extracting the incident wave angle by limited RSS information in non-ideal A2A networks is a big step for both communication and sensing applications. It enables the followings that can be studied in further detail,

- Demonstrates global observability to assure controllability on non-linear dynamic systems,
- Eliminates the requirement for the position information of the mutual, and make relative position estimation possible in radio localization systems,

- Keeps the connectivity by lowering antenna impact on the channel without external aid (i.e. intelligent surfaces), resulting with lower packet outages,
- Maximizes the LoS capacity for mobile A2A communication,
- Eliminates the requirement of the orientation and position information for the sake of sustainable physical channel,
- Provides secure communication by detecting unauthorized incident wave from unexpected angles,
- Adapts the A2A network for wide range of channel fading distributions in directional communication in THz band by beamforming and beamfocusing,
- Decreases the co-channel interference and electromagnetic interference by increasing the radiation efficiency,
- Enables the use of different data driven models for wave angle estimation with different application needs.

## VII. CONCLUSION

In conclusion, a thorough 3D geometry based A2A link under a dynamic antenna with alignment, field pattern and polarization imperfections has been structured. Under these antenna imperfections, RSS has been exploited to estimate incident wave angles by using the L2L concept of MAML that can be generalized for any A2A fading channel with less than  $10^5$  limited amount of data. Going one step further, FOMAML with less computation requirement has been deployed to cross the limits of meta-optimization for incident wave angle estimation, utilizing only first order gradient. An upper bound for the MAML accuracy have been established to compare several case demonstrations. It has been observed that radiation intensity on a fading channel has a vital impact on 3D perspective, even if the radiator is an ideal omnidirectional antenna. MAML can reach up to 0.85 training accuracy and 0.754 incident elevation angle accuracy 0.722 incident azimuth angle accuracy under the mentioned antenna imperfections, whilst CNN barely converges with 0.16 incident elevation angle accuracy using same dataset. On the other hand, DenseNet manages the learning with reaching up to 40% in DenseNet-5, yet still fails in the evaluation for unseen tasks. Furthermore, FOMAML has the fastest convergence rate for limited iteration, yet it fails to reach MAML capabilities with the same shot and class configuration. Lastly, we present our vision of the potential usage of the proposed end-to-end model.

## APPENDIX A

The radiation power density  $P_r = \frac{1}{2}\Re[\mathbf{E} \times \mathbf{H}^*]$  and the radiation intensity  $U$  relation is following

$$P_r = \frac{1}{d^2}U(\psi, \theta), \text{ W/m}^2 \quad (54)$$

The superimposed electrical field ( $\mathbf{E}(r, \theta, \psi)$ ) components are following

$$E_\theta \approx j\eta \frac{k_w I_0 L e^{-jkd}}{4\pi d} \sin \theta, \quad (55)$$

$$E_r \approx E_\psi = 0, \quad (56)$$

where  $\eta$  is intrinsic impedance and  $k_w = \frac{2\pi}{\lambda}$  is the wave number for the antenna with  $I_0$  current density. Note that due

to the far-field assumption, the relation between  $\mathbf{E}$  and  $\mathbf{H}$  is linear with  $\eta$ . Therefore,  $U = \frac{d^2}{2\eta}|\mathbf{E}|^2$  is a function of  $E_\theta$  solely, where the  $\mathbb{E}(E_\theta) \approx \sin \theta$ . The updated radiation density is the following

$$U(\theta) = \frac{d^2}{2\eta}|E_\theta|^2 = \eta \frac{k_w^2 (I_0 L)^2}{32\pi^2} \sin^2 \theta \quad (57)$$

$$\mathbb{E}(U(\theta)) = \sin^2 \theta \quad (58)$$

Therefore, the directivity of the antenna ( $D = \frac{\max U}{U_0}$ ) with  $\phi_{T,R}^{\psi, \theta}$  is following

$$D(\psi, \theta) = 4\pi \frac{\max U(\psi, \theta)}{P_r} = 4\pi \frac{\max U(\theta)}{P_r}. \quad (59)$$

where  $U_0$  is the isotropic source radiation density.

## REFERENCES

- [1] N. Goddemeier and C. Wietfeld, "Investigation of air-to-air channel characteristics and a UAV specific extension to the Rice model," in *IEEE Globecom Workshops*, pp. 1–5, 2015.
- [2] Z. Chen, G. Gokeda, and Y. Yu, *Introduction to Direction-of-Arrival Estimation*. Artech House, 2010.
- [3] M. S. Ullah, A. Tewfik, and R. W. Heath, "Power scalable angle of arrival estimation using pilot design with orthogonal subsequences," *IEEE Open Journal of the Communications Society*, vol. 2, pp. 1690–1709, 2021.
- [4] E. Gentilho Jr, P. R. Scalassara, and T. Abrão, "Direction-of-arrival estimation methods: A performance-complexity tradeoff perspective," *Journal of Signal Processing Systems*, vol. 92, no. 2, pp. 239–256, 2020.
- [5] M. Malajner, P. Planinsic, and D. Gleich, "Angle of arrival estimation using RSSI and omnidirectional rotatable antennas," *IEEE Sensors Journal*, vol. 12, no. 6, pp. 1950–1957, 2011.
- [6] B. Hua and et al., "Channel modeling for UAV-to-ground communications with posture variation and fuselage scattering effect," *IEEE Transactions on Communications*, 2023.
- [7] X. Mao, C.-X. Wang, and H. Chang, "A 3D non-stationary geometry-based stochastic model for 6G uav air-to-air channels," in *IEEE International Conference on Wireless Communications and Signal Processing (WCSP)*, pp. 1–5, 2021.
- [8] J. Zhao, F. Gao, W. Jia, W. Yuan, and W. Jin, "Integrated sensing and communications for UAV communications with jittering effect," *IEEE Wireless Communications Letters*, vol. 12, no. 4, pp. 758–762, 2023.
- [9] R. K. Miranda, D. A. Ando, J. P. C. da Costa, and M. T. de Oliveira, "Enhanced direction of arrival estimation via received signal strength of directional antennas," in *IEEE International Symposium on Signal Processing and Information Technology (ISSPIT)*, pp. 162–167, 2018.
- [10] X. Cheng, F. Shu, Y. Li, Z. Zhuang, D. Wu, and J. Wang, "Optimal measurement of drone swarm in RSS-based passive localization with region constraints," *IEEE Open Journal of Vehicular Technology*, vol. 4, pp. 1–11, 2022.
- [11] W. Zhang and W. Zhang, "An efficient UAV localization technique based on particle swarm optimization," *IEEE Transactions on Vehicular Technology*, vol. 71, no. 9, pp. 9544–9557, 2022.
- [12] X. Feng, K. A. Nguyen, and Z. Luo, "A survey of deep learning approaches for WiFi-based indoor positioning," *Journal of Information and Telecommunication*, vol. 6, no. 2, pp. 163–216, 2022.
- [13] N. Wu, X. Wang, B. Lin, and K. Zhang, "A CNN-based end-to-end learning framework toward intelligent communication systems," *IEEE Access*, vol. 7, pp. 110 197–110 204, 2019.
- [14] F.-L. Luo, *Machine Learning for Future Wireless Communications*. John Wiley & Sons, 2020.
- [15] H. Feng, S. Huang, and D.-X. Zhou, "Generalization analysis of CNNs for classification on spheres," *IEEE Transactions on Neural Networks and Learning Systems*, 2021.
- [16] B. Swiderski et al., "Random CNN structure: Tool to increase generalization ability in deep learning," *Eurasip Journal on Image and Video Processing*, vol. 2022, no. 1, p. 3, 2022.
- [17] G. Huang, Z. Liu, L. Van Der Maaten, and K. Q. Weinberger, "Densely connected convolutional networks," in *Proceedings of the IEEE conference on computer vision and pattern recognition*, pp. 4700–4708, 2017.
- [18] J. Vanschoren, "Meta-learning," *Automated machine learning: methods, systems, challenges*, pp. 35–61, 2019.



- [19] M. Andrychowicz *et al.*, “Learning to learn by gradient descent by gradient descent,” *Advances in Neural Information Processing Systems*, vol. 29, 2016.
- [20] C. Finn, P. Abbeel, and S. Levine, “Model-agnostic meta-learning for fast adaptation of deep networks,” in *International Conference on Machine Learning*, pp. 1126–1135, 2017.
- [21] N. L. Johannsen, S. Alkubti Almasri, and P. A. Hoeher, “Geometry-based UAV MIMO channel modeling and pattern optimization for multimode antennas,” *IEEE Transactions on Antennas and Propagation*, vol. 70, no. 11, pp. 11 024–11 032, 2022.
- [22] A. Salari and D. Erricolo, “Unmanned aerial vehicles for high-frequency measurements: An accurate, fast, and cost-effective technology,” *IEEE Antennas and Propagation Magazine*, vol. 64, no. 1, pp. 39–49, 2021.
- [23] A. Y. Umeyama, J. L. Salazar-Cerreno, and C. Fulton, “UAV-based antenna measurements for polarimetric weather radars: Probe analysis,” *IEEE Access*, vol. 8, pp. 191 862–191 874, 2020.
- [24] T. Zhou, B. Hua, Q. Zhu, H. Ni, K. Mao, and X.-M. Chen, “Spatial-temporal correlations of U2V channel considering fuselage posture and antenna pattern,” in *European Conference on Antennas and Propagation (EuCAP)*, pp. 1–5, 2022.
- [25] S. J. Maeng, H. Kwon, O. Ozdemir, and I. Güvenç, “Impact of 3D antenna radiation pattern in UAV air-to-ground path loss modeling and RSRP-based localization in rural area,” *IEEE Open Journal of Antennas and Propagation*, vol. 4, pp. 1029–1043, 2023.
- [26] H. Du, W. Wang, C. Xu, R. Xiao, and C. Sun, “Real-time onboard 3D state estimation of an unmanned aerial vehicle in multi-environments using multi-sensor data fusion,” *Sensors*, vol. 20, no. 3, p. 919, 2020.
- [27] K. Gamagedara, T. Lee, and M. Snyder, “Quadrotor state estimation with IMU and delayed real-time kinematic GPS,” *IEEE Transactions on Aerospace and Electronic Systems*, vol. 57, no. 5, pp. 2661–2673, 2021.
- [28] J. Zhao, W. Jia, F. Zhang, F. He, W. Jin, and N. Jiang, “Joint state estimation with integrated sensing and communications for UAV enabled 6G systems,” *Electronics Letters*, vol. 59, no. 2, 2023.
- [29] S. Wang, Y. Wang, X. Bai, and D. Li, “Communication efficient, distributed relative state estimation in UAV networks,” *IEEE Journal on Selected Areas in Communications*, vol. 41, no. 4, pp. 1151–1166, 2023.
- [30] N. Bniam, A. Aerts, D. Joosens, J. Steckel, and M. Weyn, “RSS-based AoA estimation system for IoT applications using Rotman lens,” in *European Conference on Antennas and Propagation (EuCAP)*, pp. 1–5, 2020.
- [31] S. Tomic, M. Beko, R. Dinis, and L. Bernardo, “On target localization using combined RSS and AoA measurements,” *Sensors*, vol. 18, no. 4, pp. 1–25, 2018.
- [32] A. W. Long, K. C. Wolfe, M. J. Mashner, and G. S. Chirikjian, “The banana distribution is Gaussian: A localization study with exponential coordinates,” in *Robotics: Science and Systems VIII*. The MIT Press, 07 2013.
- [33] O. A. Amodu, C. Jarray, S. A. Busari, and M. Othman, “Thz-enabled uav communications: Motivations, results, applications, challenges, and future considerations,” *Ad Hoc Networks*, vol. 140, pp. 1–17, 2023.
- [34] R. Yang, Z. Zhang, X. Zhang, C. Li, Y. Huang, and L. Yang, “Meta-learning for beam prediction in a dual-band communication system,” *IEEE Transactions on Communications*, vol. 71, no. 1, pp. 145–157, 2022.
- [35] J. Xia and D. Gunduz, “Meta-learning based beamforming design for MISO downlink,” in *IEEE International Symposium on Information Theory (ISIT)*, pp. 2954–2959, 2021.
- [36] Y. Wang, M. Chen, Z. Yang, W. Saad, T. Luo, S. Cui, and H. V. Poor, “Meta-reinforcement learning for reliable communication in THz/VLC wireless VR networks,” *IEEE Transactions on Wireless Communications*, vol. 21, no. 9, pp. 7778–7793, 2022.
- [37] M. Khoshboresh-Masouleh and R. Shah-Hosseini, “Multimodal few-shot target detection based on uncertainty analysis in time-series images,” *Drones*, vol. 7, no. 2, p. 66, 2023.
- [38] M. Wu, F. Jiang, J. Liu, and Y. Peng, “Application of CIDAE-ANIL in end-to-end communication of IRS-assisted UAV system,” *IEEE Access*, vol. 10, pp. 80 703–80 713, 2022.
- [39] A. Y. Majid, S. Saaybi, V. Francois-Lavet, R. V. Prasad, and C. Verhoeven, “Deep reinforcement learning versus evolution strategies: A comparative survey,” *IEEE Transactions on Neural Networks and Learning Systems*, pp. 1–19, 2023, (Early Access).
- [40] L. Chen *et al.*, “Learning with limited samples: Meta-learning and applications to communication systems,” *Foundations and Trends in Signal Processing*, vol. 17, no. 2, pp. 79–208, 2023.
- [41] E. Yel and N. Bezzo, “A meta-learning-based trajectory tracking framework for UAVs under degraded conditions,” in *IEEE/RSJ International Conference on Intelligent Robots and Systems (IROS)*, pp. 6884–6890, 2021.
- [42] I. Mallioras, Z. D. Zaharis, P. I. Lazaridis, and S. Pantelopoulou, “A novel realistic approach of adaptive beamforming based on deep neural networks,” *IEEE Transactions on Antennas and Propagation*, vol. 70, no. 10, pp. 8833–8848, 2022.
- [43] S. Li, Z. Liu, S. Fu, Y. Wang, and F. Xu, “Intelligent beamforming via physics-inspired neural networks on programmable metasurface,” *IEEE Transactions on Antennas and Propagation*, vol. 70, no. 6, pp. 4589–4599, 2022.
- [44] B. Luijten *et al.*, “Deep learning for fast adaptive beamforming,” in *IEEE International Conference on Acoustics, Speech and Signal Processing (ICASSP)*, pp. 1333–1337, 2019.
- [45] D. Tse and P. Viswanath, *Fundamentals of Wireless Communication*. Cambridge University Press, Section 2.2.3, 2005.
- [46] S. O. Al-Jazzar, Z. Hamici, and S. Aldalameh, “Two-dimensional AOA estimation based on a constant modulus algorithm,” *International Journal of Antennas and Propagation*, vol. 2017, pp. 1–6, 2017.
- [47] C. Wu and J. Elangage, “Multiemitter two-dimensional angle-of-arrival estimator via compressive sensing,” *IEEE Transactions on Aerospace and Electronic Systems*, vol. 56, no. 4, pp. 2884–2895, 2019.
- [48] R. G. Gallager, *Stochastic processes: theory for applications*. Cambridge University Press, 2013.
- [49] J. Ruze, “The effect of aperture errors on the antenna radiation pattern,” *Il Nuovo Cimento*, vol. 9, no. 3, pp. 364–380, 1952.
- [50] M. Badi, J. Wensowitch, D. Rajan, and J. Camp, “Experimentally analyzing diverse antenna placements and orientations for UAV communications,” *IEEE Transactions on Vehicular Technology*, vol. 69, no. 12, pp. 14 989–15 004, 2020.
- [51] T. Namiki, Y. Murayama, and K. Ito, “Improving radiation-pattern distortion of a patch antenna having a finite ground plane,” *IEEE Transactions on Antennas and Propagation*, vol. 51, no. 3, pp. 478–482, 2003.
- [52] C. A. Balanis, *Antenna Theory: Analysis and Design*. John Wiley & Sons, 2015.
- [53] Y. S. Abu-Mostafa, M. Magdon-Ismael, and H.-T. Lin, *Learning from Data*. AMLBook New York, 2012.
- [54] X. A. F. Cabezas, D. P. M. Osorio, and M. Juntti, “A framework for uav-based distributed sensing under half-duplex operation,” *arXiv preprint arXiv:2302.10673*, 2023.
- [55] A. Nichol, J. Achiam, and J. Schulman, “On first-order meta-learning algorithms,” *arXiv preprint arXiv:1803.02999*, 2018.
- [56] S. Park, O. Simeone, and J. Kang, “Meta-learning to communicate: Fast end-to-end training for fading channels,” in *IEEE International Conference on Acoustics, Speech and Signal Processing (ICASSP)*, pp. 5075–5079, 2020.
- [57] R. Kumar, T. Deleu, and Y. Bengio, “The effect of diversity in meta-learning,” in *Proceedings of the AAAI Conference on Artificial Intelligence*, vol. 37, no. 7, pp. 8396–8404, 2023.
- [58] A. Owfi, C. Lin, L. Guo, F. Afghah, J. Ashdown, and K. Turck, “A meta-learning based generalizable indoor localization model using channel state information,” in *IEEE Global Communications Conference*, pp. 4607–4612, 2023.
- [59] A. Rajeswaran, C. Finn, S. M. Kakade, and S. Levine, “Meta-learning with implicit gradients,” *Advances in neural information processing systems*, vol. 32, 2019.



**Eray Güven** (guven.eray@polymtl.ca) received his B.S. degree in Electronics and Communication Engineering at Istanbul Technical University, Turkey in 2021. He is currently studying for a Ph.D. degree in electrical engineering at Polytechnique Montréal, Montréal, Canada.



**Güneş Karabulut Kurt** (gunes.kurt@polymtl.ca), IEEE Senior Member, is a Canada Research Chair (Tier 1) in New Frontiers in Space Communications and Associate Professor at Polytechnique Montréal, Montréal, QC, Canada. From 2010 to 2021, she was a professor at Istanbul Technical University. She is a Marie Curie Fellow and has received the Turkish Academy of Sciences Outstanding Young Scientist (TÜBA-GEBIP) Award in 2019. She received her Ph.D. degree in electrical engineering from the University of Ottawa, ON, Canada. Her research interests include multi-functional space networks, space security, and wireless testbeds.